BIOCHEMISTRY
including biophysical chemistry & molecular biology

Article

pubs.acs.org/biochemistry

Second-Sphere Interactions between the C93−Y157 Cross-Link and the Substrate-Bound Fe Site Influence the O_2 Coupling Efficiency in Mouse Cysteine Dioxygenase

Wei Li,[†] Elizabeth J. Blaesi,[‡] Michael D. Pecore,[†] Joshua K. Crowell,[†] and Brad S. Pierce*[,†]

[†]Department of Chemistry and Biochemistry, College of Sciences, The University of Texas at Arlington, Arlington, Texas 76019, United States

[‡]Department of Chemistry, University of Wisconsin—Madison, Madison, Wisconsin 53706, United States

Supporting Information

ABSTRACT: Cysteine dioxygenase (CDO) is a non-heme iron enzyme that catalyzes the O_2-dependent oxidation of L-cysteine (L-Cys) to produce cysteinesulfinic acid (CSA). Adjacent to the Fe site of CDO is a covalently cross-linked cysteine−tyrosine pair (C93−Y157). While several theories have been proposed for the function of the C93−Y157 pair, the role of this post-translational modification remains unclear. In this work, the steady-state kinetics and O_2/CSA coupling efficiency were measured for wild-type CDO and selected active site variants (Y157F, C93A, and H155A) to probe the influence of second-sphere enzyme−substrate interactions on catalysis. In these experiments, it was observed that both k_{cat} and the O_2/CSA coupling efficiency were highly sensitive to the presence of the C93−Y157 cross-link and its proximity to the substrate carboxylate group. Complementary electron paramagnetic resonance (EPR) experiments were performed to obtain a more detailed understanding of the second-sphere interactions identified in O_2/CSA coupling experiments. Samples of the catalytically inactive substrate-bound Fe^{III}−CDO species were treated with cyanide, resulting in a low-spin ($S = {}^1/_2$) ternary complex. Remarkably, both the presence of the C93−Y157 pair and interactions with the Cys carboxylate group could be readily identified by perturbations to the rhombic EPR signal. Spectroscopically validated active site quantum mechanics/molecular mechanics and density functional theory computational models are provided to suggest a potential role for Y157 in the positioning of the substrate Cys in the active site and to verify the orientation of the **g**-tensor relative to the CDO Fe site molecular axis.

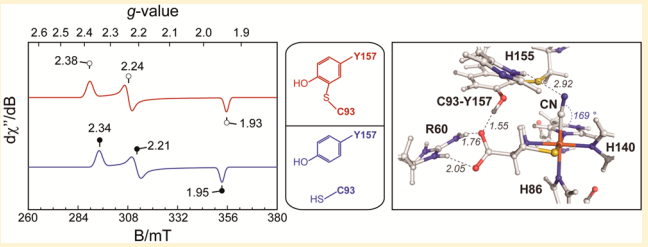

Enzymes involved in sulfur oxidation and transfer are increasingly being recognized as potential drug targets for the development of antimicrobials and therapies for both cancer and inflammatory disease.[1−4] Ironically, while sulfur is considered one of the six primordial elements required during the early stages of biological evolution, mechanistic characterization of enzymes involved in sulfur metabolism is far from complete. The study of enzymes involved in mammalian sulfur metabolism has been of considerable medical interest recently because of the observation that patients suffering from neurological disorders, such as autism and Down syndrome, have significantly lower plasma concentrations of transsulfuration pathway and methionine cycle products [cysteine (Cys), homocysteine (HCY), glutathione (GSH), and *S*-adenosylmethionine (SAM)].[5,6] Imbalances in Cys metabolism have also been observed in a variety of other neurological disorders such as motor neuron disease, Parkinson's disease, and Alzheimer's disease.[7−9] These observations suggest a potential correlation between impaired sulfur metabolism, oxidative stress, and neurodegenerative disease.[5] Cysteine dioxygenase (CDO) and cysteamine (2-aminoethanethiol) dioxygenase (ADO) are the only known mammalian thiol dioxygenase (TDO) enzymes. TDO enzymes use a single Fe(II) ion within their active site to catalyze the O_2-dependent oxidation of sulfur-containing amino acid derivatives without the need for an external electron source. Of the TDO enzymes, CDO is the best characterized. Scheme 1 illustrates the reaction catalyzed by CDO. Until recently, the catabolic dissimilation of Cys to produce inorganic sulfate, pyruvate, hypotaurine, and taurine was believed to be unique within the domain of eukaryotes.[10,11] However, a number of bacterial TDO enzymes have now been identified,

Scheme 1. Reaction Catalyzed by CDO

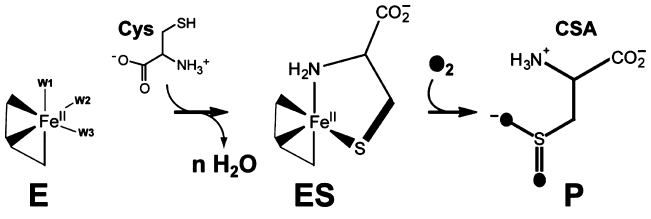

Received: July 29, 2013
Revised: November 7, 2013
Published: November 26, 2013

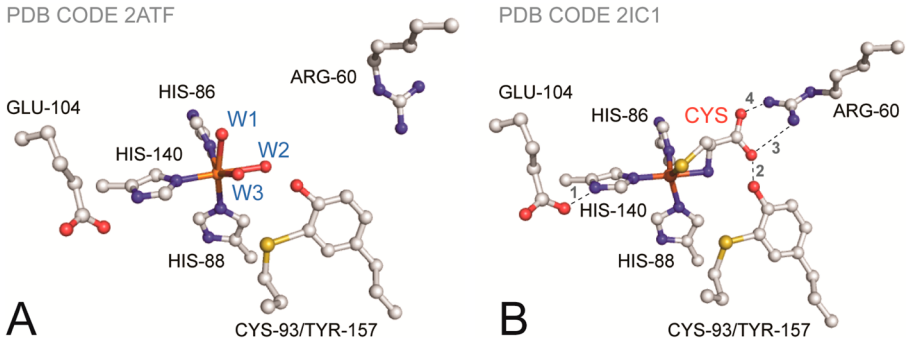

Figure 1. (A) Crystal structure (1.75 Å resolution) of resting CDO (PDB entry 2ATF).[14] Active site solvent ligands are designated W1−W3. (B) Crystal structure (2.7 Å resolution) of the substrate-bound CDO active site (PDB entry 2IC1). Selected distances indicated by 1−4 are 2.70, 2.75, 2.88, and 2.27 Å, respectively.[14,15]

suggesting that the ability to oxidize excess thiols is advantageous for survival.

While multiple high-resolution crystal structures of mammalian CDO have been determined [Protein Data Bank (PDB) entries 2ATF, 2B5H, and 2IC1],[8,12,13] mechanistic details are limited for this emerging class of enzymes. As illustrated in Figure 1, the active site of CDO contains a ferrous iron ligated by the N_ε atoms of His86, His88, and His140, representing a new three-His variant on the classic two-His, one-carboxylate facial triad observed in mononuclear non-heme iron enzymes.[8,14−16] Within the non-heme mononuclear iron family, only a handful of enzymes with a three-His active site motif have been crystallographically characterized [CDO, diketone dioxygenase (Dke1),[17] and gentisate 1,2-dioxygenase (GDO)[18]]. However, on the basis of sequence homology, it has been proposed that ADO also contains a three-His non-heme iron active site.[19]

The study of non-heme iron enzymes has historically attracted considerable interest in the realm of bioinorganic chemistry. This intense focus of research efforts can largely be explained by the vast number of functionally (and structurally) diverse non-heme iron enzymes identified throughout the biological kingdom, and the incredible versatility exhibited in chemical oxidations they initiate (mono- and dioxygenations, aliphatic desaturation, halogenations, and oxidative ring cyclizations).[20−25] Remarkably, all of these divergent oxidations are facilitated by minor perturbations to what is essentially a conserved first coordination sphere to a mononuclear Fe(II) active site. With the notable exceptions mentioned above and the aliphatic halogenase enzyme (SyrB2), the typical Fe(II) coordination sphere observed for this class of enzymes is comprised of two protein-derived neutral His residues and one monoanionic carboxylate ligand provided by either an Asp or Glu residue. Because all protein-derived ligands occupy one face of an octahedron, the substrate/cofactor binding and O_2 binding occur at the opposite octahedral face of the two-His, one-carboxylate facial triad. Alternatively, within the active site of SyrB2, a single chloride anion (Cl^-) replaces the protein-derived carboxylate ligand. This unusual Fe coordination is responsible for the "chloride rebound" mechanism resulting in chlorination of the terminal methyl group of amino acids covalently attached to peptidyl carrier proteins (PCPs).[26,27] As with other members of this enzymatic family, the Fe site within SyrB2 is also coordinated by a monoanionic ligand set. In contrast to this monoanionic facial triad motif, the active site of CDO (and potentially ADO) contains a neutral all-His (three-His) facial triad.

In addition to the three-His active site coordination, crystal structures of recombinant CDO reveal a covalently cross-linked cysteine−tyrosine pair (C93−Y157) within 3.3 Å of the iron center. To date, relatively few enzymes have been identified with an analogous post-translational modification.[28−31] A number of theories have been proposed for the function of the C93−Y157 pair; however, self-oxidation of endogenous residues adjacent to oxidase and oxygenase non-heme iron centers is commonly observed. For example, the irreversible self-hydroxylation of Tyr73 within TauD during the O_2- and α-ketogluterate-dependent oxidation of taurine is responsible for oxidative inactivation of this enzyme over multiple catalytic turnovers.[32,33] Similar self-oxidation behavior has been observed for the two-His, one-carboxylate non-heme iron enzymes prolyl-4-hydroxylase and lysyl hydroxylase.[34−36] By analogy to the self-hydroxylation pathway of TauD, it is possible that formation of the C93−Y157 pair in CDO is simply the result of uncoupled turnover and is not relevant to native catalysis. In apparent support of this hypothesis, it has been reported that the C93−Y157 cross-link forms over hundreds of catalytic turnovers in the presence of excess Fe, Cys, and O_2.[37] Contrary to this hypothesis, the C93A variant of CDO, which is unable to produce the C93−Y157 cross-link, is catalytically active, albeit with decreased activity.[15] Moreover, it has been previously demonstrated that the specific activity of wild-type CDO increases in a manner concomitant with C93−Y157 cross-link formation.[37,38] In the face of these observations, it is clear that further investigation into the relevance of this enigmatic post-translational modification to native catalysis is necessary.

Among mononuclear dioxygenase enzymes, second-sphere residues are frequently employed to modulate the reactivity of transient Fe−oxo intermediates during catalysis. For example, within the active site of 2,3-dioxygenase, a second-sphere histidine residue (H200) has been identified to have a profound influence on the enzymatic steps following O_2 activation.[39] Indeed, selected H200 variants (H200F and H200N) exhibit increased transient intermediate stability[39,40] and divergent substrate oxidation mechanisms (intradiol vs extradiol) relative to that of the wild-type enzyme.[41] By extension, it is reasonable to assume that second-sphere interactions also play a crucial role in regulating thiol oxidation by non-heme iron enzymes. Unlike C93, both Y157 and H155 are universally conserved among CDO enzymes.[10] Therefore, these residues make an attractive starting point for the exploration of key second-sphere interactions relevant to native CDO catalysis.

dx.doi.org/10.1021/bi4010232 | *Biochemistry* 2013, 52, 9104−9119

Conveniently, CDO can be prepared with variable amounts of the C93−Y157 cross-link present. For example, the as-isolated CDO (termed AI-CDO) typically contains ∼50 ± 10% C93−Y157 cross-link as determined by sodium dodecyl sulfate−polyacrylamide gel electrophoresis (SDS−PAGE) densitometry. However, if the enzyme is allowed to turn over with excess L-Cys, a nearly quantitative yield of the C93−Y157 pair is generated within purified CDO. For the sake of clarity, the fully modified enzyme prepared by this method is designated α-CDO. Therefore, the influence of the C93−Y157 pair can be investigated within the wild-type enzyme by comparison of AI-CDO with α-CDO. Selected CDO variants (C93A, Y157F, and H155A) were also prepared for comparison to the wild-type enzyme isoforms.

The efficiency at which an oxygenase enzyme incorporates 1 mol of O_2 into the product is commonly termed "coupling". In the steps following O_2 activation, unregulated access of solvent molecules to transient Fe−oxo intermediates generated prior to substrate oxidation often results in unproductive or uncoupled catalysis. The outcome of enzymatic uncoupling can result in oxidation of amino acid residues adjacent to the non-heme iron center, formation of reactive oxygen species (ROS), and ultimately enzymatic inactivation.[35] As a general rule, to limit enzymatic uncoupling, oxygenase enzymes utilize second-sphere interactions to tightly regulate solvent access within the active site. As illustrated in Figure 1, the distance separating the second-sphere C93−Y157 hydroxyl group from the carboxylate group of the Fe-bound substrate (L-Cys) is 2.75 Å. However, as stated previously, the relevance of this second-sphere interaction to native catalysis is poorly understood. In this work, the steady-state rate of CSA formation and O_2 consumption were simultaneously monitored to explore the effect of the C93−Y157 post-translational modification on native catalysis and O_2/CSA coupling efficiency for CDO.

In practice, CSA/O_2 coupling experiments are useful for the identification of key enzyme−substrate interactions relevant to native catalysis. However, once identified, more sophisticated methods are needed to develop a "molecular-level" understanding of these substrate−enzyme interactions. Therefore, complementary EPR experiments were performed utilizing the catalytically inactive Fe^{III}−CDO species in which cyanide was used as a spectroscopic probe to monitor the effect of the C93−Y157 pair on the electronic structure of the substrate-bound active site. Here, the strong π-accepting character of cyanide is exploited to produce a low-spin cyano/substrate-bound Fe^{III}−CDO complex. To aid in the interpretation of these EPR spectra, as well as to gain further insight into the electronic structure of the active site in the absence or presence of the C93−Y157 cross-link, we used whole-protein QM/MM computational models and DFT calculations. Together, the kinetic, spectroscopic, and computational results all lend support to the hypothesis that the cross-link plays a vital role in CDO-mediated catalysis.

MATERIALS AND METHODS

Purification. Recombinant mouse CDO (EC 1.13.11.20) was expressed in *Escherichia coli* BL21(DE3) pLysS competent cells (Novagen) and purified as previously described.[42,43] Tobacco etch virus protease (TEV) was used to cleave CDO from the maltose binding protein (MBP) fusion protein (4 h at ambient temperature) in 50 mM HEPES, 100 mM NaCl, and 0.3 mM tris(2-carboxyethyl)phosphine hydrochloride (TCEP) (pH 7.5). Subtractive Ni-IMAC (GE Healthcare, 5 mL HiTrap IMAC FF) was used to separate MBP from CDO. The concentration of CDO protein was determined using the published extinction coefficient at 280 nm (28300 M^{-1} cm^{-1}).[38] Because incorporation of Fe within AI-CDO is variable from batch to batch (60−80%), each preparation was assayed for both ferrous and ferric iron spectrophotometrically as described previously.[43,44] In a typical preparation of CDO, 90−95% of the iron is observed as ferrous. For the sake of clarity, the concentrations reported in enzymatic assays reflect the concentration of ferrous iron within samples of CDO (Fe^{II}−CDO). The fraction of CDO containing the C93−Y157 thioether linkage was determined by SDS−PAGE densitometry using the freely available ImageJ software (http://rsbweb.nih.gov/ij/index.html). AI-CDO prepared from a 10 L fermentation typically contained 50 ± 10% C93−Y157 cross-link as observed by SDS−PAGE. Broad-range protein molecular weight markers (catalog no. V8491) utilized in SDS−PAGE experiments were purchased from Promega (Madison, WI).

All CDO variants (C93A, Y157F, and H155A) were prepared using the QuikChange Lightning Site-Directed Mutagenesis kit (Agilent Technologies). Mutagenic primers were purchased from Integrated DNA Technologies (https://www.idtdna.com), and sequence verification of single-amino acid mutations was performed by Sequetech (Mountain View, CA).

Conversion of AI-CDO to Fully Modified CDO (α-CDO). Typically, ∼100−200 μM AI-CDO was added to a buffered solution [25 mM HEPES and 50 mM NaCl (pH 7.5)] containing excess Cys (25 mM). This solution was allowed to react for ∼30 min at 37 °C, prior to buffer exchange with a Sephadex G-25 desalting column or overnight dialysis at 4 °C. Following buffer exchange, the protein was concentrated using an Amicon N_2 stirred cell equipped with an YM-10 ultrafiltration membrane (Millipore). The ferrous and ferric iron content and complete C93−Y157 cross-link formation were confirmed spectrophotometrically and by SDS−PAGE, respectively, as described above. The specific activity of all CDO preparations was verified as described below.

HPLC CDO Activity Assay. Cysteinesulfinic acid (CSA) was assayed using a modified version of the HPLC method described previously.[43] The mobile phase [20 mM sodium acetate, 0.6% methanol, and 1% heptofluorobutyric acid (pH 2.0)] was altered to compensate for a change in the reverse-phase column (Phenomenex Kinetex C18, 100 Å column, 100 mm × 4.6 mm, 2.6 μm). Sample injections (50 μL) were eluted isocratically at a flow rate of 1.0 mL/min and detected at 218 nm. This modification to the HPLC method resulted in greater column retention of CSA, allowing for separation of CSA from the void volume. In a typical assay, 1 μM CDO was added to a solution of L-Cys (0.1−25 mM) under aerobic conditions at 37 °C. Aliquots were taken from each reaction mixture at selected time points and reactions quenched by spin filtration (0.22 μm cellulose acetate membrane; Corning, Spin-X) prior to HPLC analysis. This HPLC method was also used to monitor hypotaurine formation in CDO assays utilizing cysteamine (CSH) as a substrate. The concentration of CSA and hypotaurine was determined by comparison to standard calibration curves (0.1−20 mM).

Oxygen Electrode. The dioxygen concentration was determined polarographically using a standard Clark electrode (Hansatech Instruments, Norfolk, England) within a jacketed 2.5 mL cell at 37 ± 2 °C. The electrode was bathed in a saturated solution of KCl and separated from the buffer using a

gas-permeable membrane. The electrode was calibrated by measuring the deflection in the voltage upon addition of ~500 units of catalase (Sigma-Aldrich, St. Louis, MO) to a buffer with a known concentration of H_2O_2 (ε_{250} = 16.7 M^{-1} cm^{-1}). Once the reaction had reached completion, the amplitude for the change in voltage was used to determine a response factor for the electrode. As an additional control, the stability of the electrode response factor was verified for each pH used in steady-state assays (pH 5−11) by addition of sodium dithionite to aerobic buffer. Enzymatic reaction mixtures were made by adding 1 mL of reaction buffer (25 mM Good's buffer and 50 mM NaCl) containing Cys (0.1−25 mM) to the electrode cell under continuous aerobic mixing. The reaction was initiated by injection of CDO, resulting in a final enzyme concentration of 1 μM.

pH Profile Results. For steady-state analysis, 1 μM CDO was allowed to react with different concentrations of Cys in 25 mM HEPES and 50 mM NaCl (pH 7.5) at 37 °C. For experiments conducted over a broad pH range, the CDO solution was exchanged into an appropriate Good's buffer selected on the basis of its pK_a (MES, pK_a 6.1; HEPES, pK_a 7.5; CHES, pK_a 9.3). Each buffer was prepared at 25 mM and titrated to the desired pH using 1 N NaOH. As with steady-state reactions, 1 μM CDO was allowed to react with 20 mM Cys in 25 mM HEPES and 50 mM NaCl at 37 °C. Amounts of CSA produced and O_2 consumed were quantified by HPLC and oxygen electrode assays, respectively.

Analysis of Kinetic Data. Steady-state kinetics of wild-type and variant CDO were analyzed by SigmaPlot version 11 (Systat Software Inc., Chicago, IL). In the absence of substrate inhibition, initial rate data for CSA formation and O_2 consumption were fit to the Michaelis−Menten equation to obtain k_{cat} and K_M. In all assays, initial rates are normalized for Fe-containing CDO (v_0/[E]). Under conditions of substrate inhibition, initial rate data were fit to eq 1 to determine the dissociation equilibrium or inhibition constant (K_I).

$$v_0 = \frac{k_{cat}[S]}{K_M + [S] + \frac{[S]^2}{K_I}} \quad (1)$$

Spectroscopy. All UV−visible measurements were performed on an Agilent (Santa Clara, CA) 8453 photo diode array spectrometer. The sample temperature was held constant by a 13 L circulating water bath and a thermostable cell holder (89054A) with a magnetic stirrer. All measurements were taken in ES Quartz cuvettes (NSG Precision Cells, Farmingdale, NY). X-Band (9 GHz) EPR spectra were recorded on a Bruker (Billerica, MA) EMX Plus spectrometer equipped with a bimodal resonator (Bruker model 4116DM). Low-temperature measurements were taken using an Oxford ESR900 cryostat and an Oxford ITC 503 temperature controller. A modulation frequency of 100 kHz was used for all EPR spectra. All experimental data used for spin quantitation were collected under nonsaturating conditions.

Analysis of the EPR spectra utilized the general spin Hamiltonian

$$\hat{H} = \mathbf{D}\left[\hat{S}_Z^{\,2} - \frac{S(S+1)}{3}\right] + \mathbf{E}(\hat{S}_X^{\,2} + \hat{S}_Y^{\,2}) + \beta\mathbf{B}\cdot\mathbf{g}\cdot\mathbf{S} \quad (2)$$

where **D** and **E** are the axial and rhombic zero-field splitting (zfs) parameters, respectively, and **g** is the **g**-tensor.[45] In case of low-spin ferric iron ($S = {}^1/_2$), eq 2 simplifies to the following equation:

$$\hat{H} = \beta\mathbf{B}\cdot\mathbf{g}\cdot\mathbf{S} \quad (3)$$

EPR spectra were simulated and quantified using Spin Count (version 3.1.2), written by M. P. Hendrich at Carnegie Mellon University (Pittsburgh, PA). The simulations were generated with consideration of all intensity factors, both theoretical and experimental, to allow for the determination of species concentration. The only unknown factor relating the spin concentration to signal intensity was an instrumental factor that is specific to the microwave detection system. However, this was determined by a spin standard, Cu(EDTA), prepared from a copper atomic absorption standard solution purchased from Sigma-Aldrich.

The half-power microwave saturation ($P_{1/2}$) for these signals was determined using SpinCount according to eq 4.

$$\frac{S}{\sqrt{P}} = \frac{A}{\left(1 + \frac{P}{P_{1/2}}\right)^{b/2}} \quad (4)$$

The software performs least-squares fitting of the normalized derivative signal intensity (S) as a function of microwave power (P). The A term represents the normalized maximal signal amplitude. The variable b is a spectroscopic inhomogeneity factor that is characteristic of the spin packet of the observed resonance. Generally, the signal packet derived from frozen solutions and powders exhibits inhomogeneous line broadening behavior (b = 1).

Computational Methods. A quantum mechanics/molecular mechanics (QM/MM) approach as implemented in Gaussian09[46] was utilized in the optimization of full-protein models of mouse CDO. For the QM region, density functional theory (DFT) was employed in conjunction with Becke's three-parameter hybrid exchange functional with the Lee−Yang−Parr correlation functional (B3LYP),[47,48] as well as the 6-31G basis set[49] on all atoms except iron, its immediately ligated atoms, and the CN^- ligand (for which TZVP[50] was used instead). For the MM portion of the calculation, the Amber95 force field[51] was utilized. The QM/MM boundary was placed between the β- and α-carbons of the appropriate residues, using hydrogens as the link atoms. The α-carbons of the QM residues were held fixed during the optimization process.

The starting coordinates for the models investigated were derived from two X-ray crystal structures, namely, PDB entry 2IC1[15] for the QM region and PDB entry 3ELN[52] for the MM region residues. The cyanide ligand was manually added to the iron(III) center trans to H86, at an Fe−C distance of ~2 Å. Hydrogen atoms for the entire protein were added using Reduce version 3.14.[53] On the basis of inspection of potential hydrogen bonding interactions, histidine residues at positions 86, 88, 140, and 155 were singly protonated at N_δ, whereas all other histidines were singly protonated at N_ε. Residues R60, H86, H88, C93, H140, H155, and Y157 as well as Fe(III), L-Cys (or Sec), CN^-, and six crystallographically defined water molecules within 10 Å of the iron center were included in the QM region. In the case of the model not containing the Cys−Tyr cross-link, the starting coordinates for the C93 side chain were adjusted to eliminate the bond between the residues and hydrogen atoms were added to both C93 and Y157 to restore them to a pre-cross-linked protonation state.

dx.doi.org/10.1021/bi4010232 | Biochemistry 2013, 52, 9104−9119

In the generation of small active site models, residues H86, H88, and H140 as well as Fe(III), the substrate (analogue), and cyanide were excised from the optimized protein coordinates. Amino acid residues were capped as methyl groups at their β-carbon, with C−H bond lengths of ∼1.1 Å. Spin unrestricted single-point DFT calculations were conducted using Orca version 2.9 developed by F. Neese[54] and used the same functional and basis sets as the QM/MM portion of the calculation. PyMOL version 1.5.0.4[55] was utilized to generate isosurface plots of relevant MOs using an isodensity value of 0.05 arbitrary unit. EPR parameters for these models were also computed with Orca version 2.9, using the PBE0 functional[56] (or B3LYP in a separate calculation for comparative purposes) in conjunction with the TZVP basis set on all atoms except sulfur, selenium, and iron [for which IGLOO(III),[57] CP-(PPP),[58,59] and CP(PPP), respectively, were used]. These calculations included all orbitals within ±100 hartree of the HOMO−LUMO gap, and the origin of the **g**-tensor was taken to be the center of the electronic charge. A high-resolution radial grid with an integration accuracy of 7 was used for the Fe, S, and Se atoms.

RESULTS

Purification of CDO Forms and Selected Variants. Expression and isolation of the MBP−CDO fusion protein (Figure 2, lanes 2 and 3, respectively) were performed as previously described.[42] Shown in lane 4 are the two distinct CDO fractions (α and β) obtained from treating the as-isolated MBP−CDO fusion protein with tobacco etch virus (TEV) protease. For the sake of clarity, the expanded region shown in Figure 2B illustrates the two CDO isoforms (α and β) within AI-CDO. Previous experiments have confirmed that band α is the fraction of CDO enzyme with the covalent C93−Y157 pair, whereas the fraction within band β lacks this covalent modification.[15,37] As demonstrated in Figure 2, by comparing lane 4 to lane 5, we observed that nearly 100% α-CDO can be produced from β-CDO within 30 min by addition of excess L-Cys (25 mM) to isolated batches of AI-CDO (100−200 μM) at pH 7.5. This is consistent with previous reports that the C93−Y157 pair is produced over multiple turnovers with the substrate.[37,38] Unless otherwise stated, only fully modified CDO (Figure 2, lane 6) (α-CDO) will be used for the determination of steady-state kinetic parameters for the wild-type enzyme.

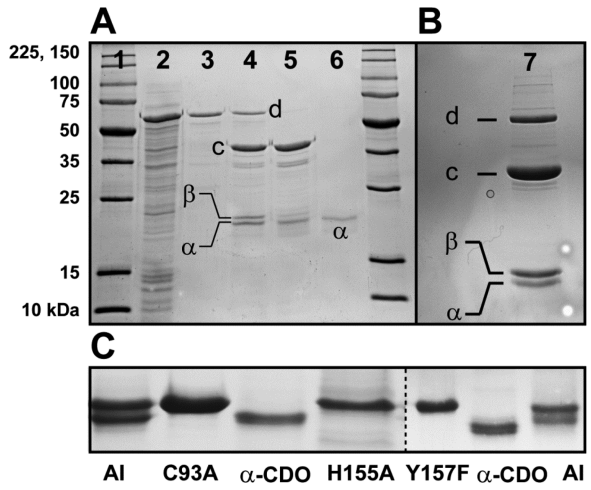

Figure 2. (A) SDS−PAGE (12%) of sequential α-CDO purification steps: lane 1, markers; lane 2, cell free extract; lane 3, purified MBP−CDO fusion protein; lane 4, MBP−CDO fusion protein following TEV protease cleavage (equivalent to lane 7 in panel B); lane 5, α-CDO produced following a 30 min treatment with excess L-Cys; lane 6, purified α-CDO following a subtractive Ni-IMAC column. (B) Lane 7 shows an expanded SDS−PAGE gel illustrating the two CDO isoforms (α and β) present in AI-CDO. The bands designated by c and d represent the cleaved maltose binding protein and the uncleaved fusion protein, respectively. (C) Migration of active site variants (C93A, H155A, and Y157F) relative to AI-CDO and α-CDO. The dashed line separates bands run on separate gels.

Because formation of the C93−Y157 pair may influence the steady-state kinetic parameters observed for CSA formation or CSA/O_2 coupling efficiency, active site variants incapable of C93−Y157 cross-link formation (namely, C93A and Y157F) were prepared to evaluate the role of the C93−Y157 pair in catalysis. Active site variants (C93A, H155A, and Y157F) were prepared using the Agilent QuikChange site-directed mutagenesis kit as described in Materials and Methods. All variants were expressed, purified, and assayed for Fe content as described above for the wild-type enzyme. Figure 2C illustrates the migration of CDO active site variants (C93A, Y157F, and H155A) relative to the as-isolated and fully modified isoforms of wild-type CDO.

Influence of the C93−Y157 Pair and Substrate Interactions on Enzymatic Coupling. Because two forms of enzyme are present (α and β) within the as-isolated enzyme, the steady-state Michaelis−Menten kinetic parameters (k_{cat} and K_M) determined for AI-CDO are not strictly valid. Therefore, coupling efficiencies were determined for α-CDO by comparing the steady-state kinetics of O_2 consumption to those of CSA formation. As described in Materials and Methods, O_2 consumption and CSA formation were measured using a calibrated Clarke-type O_2 electrode and reverse-phase HPLC, respectively. Unless otherwise noted, all initial rates are normalized for Fe-containing enzyme concentration (v_0/[E]), such that the values for k_{cat} and K_M are easily obtained from fitting the results to the Michaelis−Menten equation. The steady-state kinetics for wild-type CDO with L-Cys are shown in Figure 3A. The dashed line represents a best fit to the initial rate of O_2 consumption (●). From this analysis, the values of k_{cat} and K_M were determined to be 10.6 ± 0.4 s^{-1} and 0.7 ± 0.1 mM for the steady-state rate of O_2 consumption, respectively. In terms of O_2 consumption, the catalytic efficiency (V/K) of α-CDO is ∼15100 M^{-1} s^{-1}. By comparison, from the steady-state kinetics for CSA formation (△, solid line), k_{cat} and K_M were determined to be 8.6 ± 0.5 s^{-1} and 3.1 ± 0.6 mM, respectively (V/K ∼ 2900 M^{-1} s^{-1}). As k_{cat} represents the zero-order limit of an enzymatic reaction, the coupling efficiency can be obtained from the ratio of the k_{cat} for CSA formation to the k_{cat} for O_2 consumption. Therefore, the coupling efficiency for wild-type CDO with L-Cys is ∼81 ± 5%. A summary of kinetic parameters and CSA/O_2 coupling efficiency observed for wild-type CDO and selected active site variants is provided in Table 1. As previously stated, the steady-state kinetic parameters (k_{cat} and K_M) for AI-CDO are not strictly valid; however, by comparison to that of α-CDO, it is readily apparent that the specific activity of CDO is proportional to the extent of the C93−Y157 pair present. This observation is consistent with previous reports.[37,38] While the value obtained for K_M (with respect to CSA formation) is consistent with those typically reported for recombinant CDO, the k_{cat} for the α-CDO

dx.doi.org/10.1021/bi4010232 | Biochemistry 2013, 52, 9104−9119

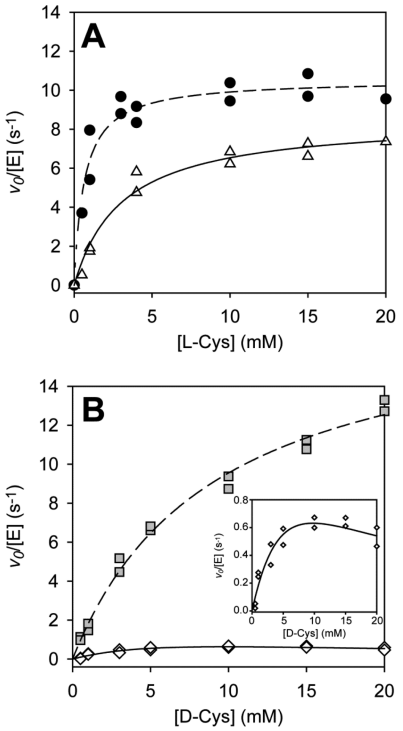

Figure 3. Steady-state kinetics of wild-type CDO-catalyzed O_2 consumption (– – –) compared to those of product formation (—) for L-cysteine (A) and D-cysteine (B). For the sake of clarity, the steady-state curve for CSA formation as a function of initial D-Cys concentration is expanded in the inset of panel B.

Table 1. Steady-State Kinetic Parameters Determined for CSA Formation and O_2 Consumption (CSA/O_2) for Selected CDO Forms and Variants

enzyme	k_{cat} (s^{-1}) (CSA/O_2)	K_M (mM) (CSA/O_2)	K_I (mM) (CSA)[b]
fully modified (α-CDO)			
L-cysteine	8.6/10.6 (81%)	3.1/0.7	–
D-cysteine	2/18.3 (4%)	8/9.1	12
as-isolated (AI-CDO)[a]	1.0–2.0 (CSA only)	4.0 (CSA only)	–
C93A	0.4/0.4 (45%)	4/4[b]	14
H155A[c]	<0.1 (CSA only)	not saturated at 25 mM	–
Y157F[c]	–	inactive	–

[a]Michaelis–Menten parameters (K_M and k_{cat}) determined for AI-CDO are not valid because two enzyme populations are present. In reality, these values represent a weighted average of the intrinsic kinetic parameters for each enzyme form (α and β). [b]The substrate inhibition constant was obtained by fitting kinetic results to the Haldane expression as described in Materials and Methods. [c]For these mutations, only the rate of CSA formation was determined.

reported here is significantly higher than those reported elsewhere.[12,15,43]

The pH dependence of CDO coupling was obtained by measuring the rate of CSA formation at a saturating Cys concentration (20 mM). As indicated by Figure 4, the optimal pH values for O_2 consumption (●, pH ~8.2) and CSA formation (△, pH 8.6) do not fully overlap. Both data sets were fit to a three-parameter normal log peak equation. For the sake of clarity, the data were normalized to the maximal k_{cat} observed for CSA formation at pH 8.6. Interestingly, the

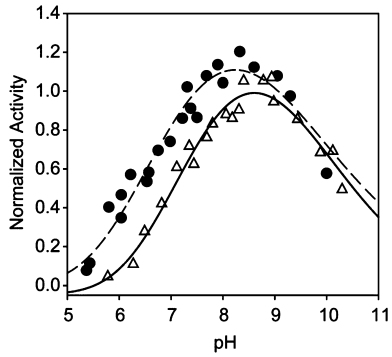

Figure 4. pH dependence of CSA/O_2 coupling efficiency for wild-type CDO with L-cysteine. For the sake of clarity, the initial rates observed for O_2 consumption (●) and CSA formation (△) were normalized to the maximal rate of CSA produced at pH 8.6.

coupling efficiency is nearly fully coupled above pH 8.5; however, under more acidic conditions (pH ≤7), CDO appears to be significantly uncoupled, with ~25 ± 10% more O_2 consumed than CSA produced.

Such coupling experiments can frequently provide greater mechanistic insight into substrate–enzyme interactions. For example, the carboxylate group of L-cysteine can potentially make two stabilizing interactions with second-sphere residues within the CDO active site (Figure 1). First, the R60 guanidinium group is at a favorable distance (2.27–2.88 Å) to stabilize the substrate carboxylate charge. Additionally, it has been proposed that the L-Cys carboxylate group may also form hydrogen bonding interactions with the nearby hydroxyl group of the C93–Y157 pair (2.75 Å). With a change in the stereochemistry of the substrate from L- to D-Cys, both H-bonding and electrostatic interactions would potentially be disrupted. As demonstrated in Figure 3B, in steady-state assays utilizing D-Cys, the maximal rate of O_2 consumption (■, dashed line) increases by nearly 2-fold (k_{cat} = 18.3 ± 0.9 s^{-1}) relative to that of the native L-Cys substrate. Additionally, the K_M for D-Cys increases to 9.1 ± 1 mM. Therefore, in terms of O_2 consumption, the catalytic efficiency observed for α-CDO with D-Cys (V/K ~ 2000 M^{-1} s^{-1}) decreases by >7-fold relative to that with L-Cys.

By contrast to what is observed for the steady-state formation of CSA from L-Cys, under identical assay conditions, α-CDO exhibits significant substrate inhibition with D-Cys [Figure 3B (◇)]. This decay is not observed in the rate of O_2 consumption, thus suggesting the formation of reactive oxygen species or self-hydroxylation during steady-state turnover. For steady-state assays exhibiting substrate inhibition, initial rates were fit to eq 1 (solid line) as described in Materials and Methods to obtain the kinetic parameters (k_{cat} = 2 s^{-1}, and K_M = 8 mM) and substrate inhibition constant (K_I = 12 mM). Given that the formation of CSA from D-Cys follows a more complicated substrate inhibition kinetic model, comparison of the k_{cat} observed for CSA formation relative to that observed for O_2 consumption is no longer valid. For the sake of simplicity, the coupling efficiency for α-CDO with D-Cys was taken as the ratio of the initial rate observed for CSA formation over that observed for O_2 consumption at a fixed and saturating substrate concentration (20 mM). By this definition, the CSA/O_2 coupling efficiency for α-CDO with D-Cys is ~4%, essentially a 20-fold decrease relative to that with the native L-Cys substrate. A similar effect on oxidative uncoupling can

dx.doi.org/10.1021/bi4010232 | Biochemistry 2013, 52, 9104–9119

also be observed in assays utilizing cysteamine (2-aminoethanethiol, CSH) as a substrate for α-CDO. Given the lack of a carboxylate group in CSH, the specific activity (v_0) of α-CDO at 20 mM CSH is vastly reduced (~0.02 s^{-1} for hypotaurine formation) relative to that of the native substrate (~0.2 s^{-1} for O_2 consumption). Moreover, the coupling efficiency (~6%) is close to that observed with D-Cys. Although coupling efficiencies have not been previously reported for this enzyme, the decreased specific activity observed for CDO with respect to D-Cys and CSH is consistent with the literature.[60−63]

The impact (if any) of the C93−Y157 post-translational modification was also interrogated by comparing the enzymatic activity and coupling efficiency of selected variants (C93A and Y157F) with those of the wild-type enzyme. As illustrated in Figure 2C, these variants are unable to produce the cross-linked pair. Interestingly, while C93 is not conserved among putative bacterial CDO enzymes, both Y157 and H155 are universally conserved.[10] Therefore, the H155A variant of CDO was also evaluated for comparison to wild-type α-CDO.

Figure 5 shows that the C93A variant is catalytically active, albeit at a level significantly decreased relative to that of the wild-type enzyme. This observation is consistent with results obtained for a similar variant (C93S and C93A) in human and rat CDO.[15,37] As with the wild-type enzyme, the rates of O_2 consumption and CSA formation are designated by a dashed line (●) and a solid line (△), respectively. Additionally, like wild-type CDO utilizing D-Cys as the substrate, the C93A variant exhibits behavior consistent with substrate inhibition, resulting in a rapid decay in the rate of CSA formation at saturating L-Cys concentrations. As observed previously, the decay in the initial rate with an increasing substrate concentration is not observed for O_2 consumption, suggesting self-oxidation and/or production of reactive oxygen species.

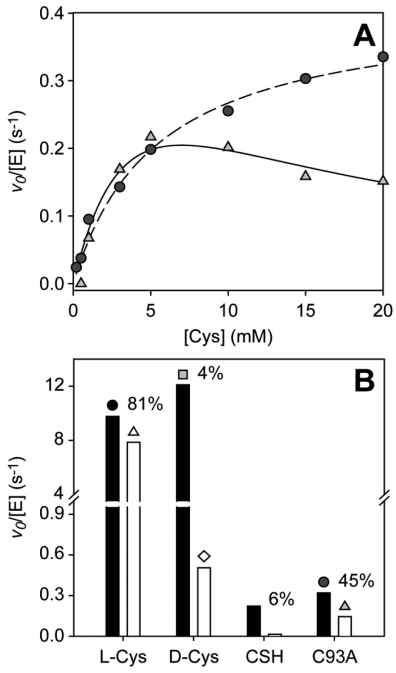

Figure 5. (A) Steady-state kinetics of C93A CDO-catalyzed O_2 consumption (●, −−−) compared to those of product formation (△, —) for L-cysteine. (B) Bar graph representing the CSA/O_2 coupling efficiency for wild-type CDO with L- and D-cysteine and cysteamine (CSH) as compared to C93A CDO with L-cysteine.

Steady-state assays of the C93A variant demonstrate a significantly lower maximal rate of O_2 consumption (k_{cat} = 0.4 s^{-1}) and Michaelis−Menten constant (K_M = 4.4 mM) relative to those of the wild-type enzyme. Alternatively, the kinetic parameters obtained for the C93A variant in terms of CSA formation were 0.4 s^{-1} (k_{cat}), 4.0 mM (K_M), and 13.5 mM (K_I). On the basis of this analysis, the CSA/O_2 coupling efficiency for the C93A variant is 43 ± 4%. Unlike experiments utilizing D-Cys or CSH, the carboxylate group of L-Cys is still present and available for interaction with R60. Therefore, the decreased level of coupling observed for the C93A variant can be attributed to disruption of second-sphere interactions with the C93−Y157 pair only. Figure 5B illustrates the coupling efficiency (percent) and observed v_0/[E] for O_2 consumption and CSA formation for the C93A variant as compared to those of the wild-type enzyme.

Although comparable to that of the wild-type enzyme in terms of iron incorporation, the specific activity of the H155A variant is nearly 2 orders of magnitude lower than that of the wild-type enzyme (~0.1 s^{-1}). Given its drastically reduced activity, the rate of product accumulation could reliably be measured only under saturating L-Cys conditions (25 mM). Isolated batches of the Y157F variant exhibited no detectable specific activity despite having appreciable ferrous iron incorporation and no visible signs of protein precipitation or denaturation.

Cyanide Binding and EPR Spectroscopy of Substrate-Bound Al-CDO, α-CDO, and the C93A Fe^{III}−CDO Complexes. In an effort to better understand the role second-sphere residues play in coupling and catalysis, the electronic structures at the active sites of catalytically relevant species of both isoforms of CDO were probed through the use of EPR spectroscopy. The parallel mode X-band EPR spectra of the substrate-bound Fe^{II}−CDO complex are characteristic of high-spin ferrous iron (S = 2) and easily differentiated from those of free hexaquaFe^{II} in solution (Figure S1 of the Supporting Information). However, in cases of systems with large spin−orbit coupling (such as CDO), the zero-field splitting (Δ_k) for the non-Kramers doublet (k) can exceed the incident microwave radiation ($\Delta_k \geq h\nu$) of the spectrometer. Therefore, at X-band frequencies ($h\nu \sim 0.3$ cm^{-1}), the majority of the resonance observed for the substrate-bound Fe^{II}−CDO complex is not observed even in the absence of an applied field (B_0 = 0).[64] In such situations, higher microwave frequencies are necessary to observe the full paramagnetic spectra. Thus, the spectroscopic intractability of the Fe^{II}−CDO signal and the high oxygen sensitivity of the substrate-bound Fe^{II}−CDO complex make EPR characterization of the catalytically active enzyme challenging. However, it has been previously demonstrated that the Fe^{II}−CDO complex can be stoichiometrically converted to the Fe^{III}−CDO complex by being treated with potassium hexachloroiridate (K_2IrCl_6).[42] While catalytically inactive, the ferric enzyme is more amenable to EPR spectroscopic characterization. In these experiments, cyanide (CN^-) was used as a spectroscopic probe to model the binding of O_2 to the substrate-bound Fe^{III}−CDO active site. The strong π-accepting character of cyanide was exploited to produce a low-spin (S = $^1/_2$) cyano/substrate-bound Fe^{III}−CDO species. In principle, the resulting ternary complex would have a formal charge and size similar to those of the proposed Fe^{III}−superoxide intermediate in the CDO catalytic cycle.[42] Thus, the Fe-bound cyano ligand could serve as a spectroscopic probe for the observation of hydrogen bonding interactions or

dx.doi.org/10.1021/bi4010232 | Biochemistry 2013, 52, 9104−9119

geometric perturbations arising from interactions with second-sphere active site residues such as the Y157 hydroxyl group of the C93−Y157 pair or the H155 imidazole ring.[15,52] Unlike π-donors such as superoxide or nitric oxide that favor a bent Fe coordination geometry, bound cyano ligands typically exhibit a strong preference for linear coordination. While this linear geometry is less desirable as a structural model for a putative Fe^{III}−superoxide intermediate, the use of cyanide as opposed to nitric oxide is spectroscopically cleaner as it prevents the production of dinitrosyl iron complexes (DNIC) (g_{obs}-values of 2.03, 2.02, and 2.01) and free nitric oxide ($g \sim 1.98$), both of which are observed at g-values comparable to those of the substrate-bound $\{FeNO\}^7$ ($S = {}^1/_2$) CDO site (g_{obs}-values of 2.07, 2.02, and 1.98).[43] Moreover, the substrate-bound CN/Cys-bound Fe^{III}−CDO complex exhibits greater g spread (Δg) than the substrate-bound $\{FeNO\}^7$ CDO, thus offering greater sensitivity to second-sphere perturbations. As with the steady-state coupling experiments, the fully modified (α-CDO), as-isolated (AI-CDO), and C93A, Y157F, and H155A forms of the enzyme were characterized for comparison.

Prior to addition of KCN, EPR spectra for both the substrate-bound α-CDO and AI Fe^{III}−CDO enzymes exhibit a sharp signal with observed g-values of 4.47, 4.36, and 4.27. A weaker set of resonances can also be observed at $g \sim 9.7$ (Figure 6A). This signal is consistent with the high-spin ($S = {}^5/_2$) substrate-bound Fe^{III}−CDO species (termed Fe^{III}−ES) previously reported.[42] Indeed, within experimental error, both the half-saturation microwave power at 10 K ($P_{1/2} \sim 90 \pm 15$ mW) and the magnitude of the axial zero-field splitting term ($|D| \sim 2.7 \pm 0.3$ cm^{-1}) are equivalent for the Fe^{III}−ES prepared from α-CDO and AI-CDO.

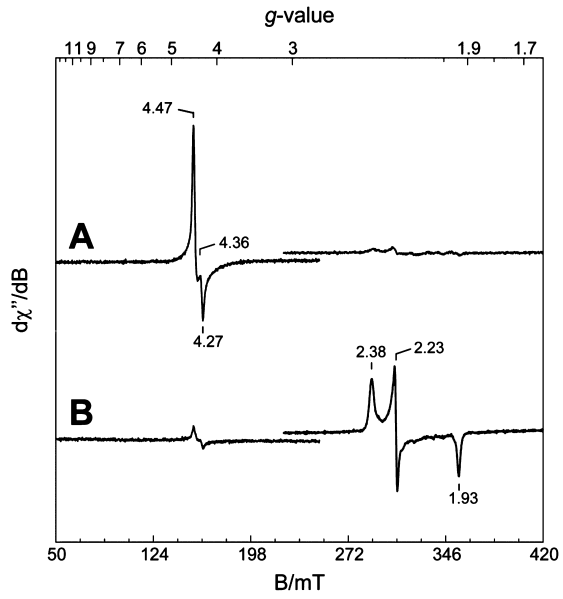

Figure 6. X-Band EPR spectra of α-Fe^{III}−ES after the addition of a KCN. Each full field spectrum for spectra A and B was collected as two independent scans to increase the number of data points and accuracy of reported g-values. For the sake of clarity, the two spectra are offset slightly. Sample conditions: 0.15 mM Fe^{III}−CDO, 0.45 mM Cys, pH 7.8 titrated with 0.5-fold (A) and 10-fold (B) molar excesses of KCN relative to Fe-containing enzyme. Instrumental parameters: microwave frequency, 9.64 GHz; modulation frequency, 100 kHz; modulation amplitude, 0.9 mT; temperature, 10 K; microwave power, 40 μW (37 dB).

However, Figure 6B shows that addition of a 10-fold molar excess of KCN relative to the α-Fe^{III}−ES enzyme (0.15 mM) results in a nearly complete loss of the high-spin EPR signal with concomitant formation of a new rhombic $S = {}^1/_2$ signal. Substoichiometric additions of cyanide relative to the Fe^{III}−ES complex (0.5-fold molar excess) resulted in only minor formation of the $S = {}^1/_2$ signal (22% of total iron) (Figure 6A), thus indicating that the α-Fe^{III}−ES enzyme has a relatively poor binding affinity for the cyanide anion. As indicated by Table 2, the g-values for this $S = {}^1/_2$ signal (2.38, 2.23, and 1.93) and half-power microwave saturation at 10 K ($P_{1/2} = 140 \pm 24$ μW; $b = 1.0$) are consistent with those observed for a variety of low-spin non-heme ferric iron enzymes. A quantitative simulation (**S1**, dashed line) for α-Fe^{III}(CN)−ES is overlaid on spectrum α in Figure 7. The spectral line width is dominated by g strain, and thus, simulations use distributions in the g-values along each principle axis (σg_1, σg_2, and σg_3) to give the correct line width. On the basis of this simulation, the concentration of CN/Cys-bound Fe^{III}−α-CDO was determined, which accounts for 91% of the initial high-spin $S = {}^5/_2$ Fe^{III}−ES signal (150 μM). Thus, nearly all of the initial high-spin α-Fe^{III}−ES is converted to the corresponding low-spin α-Fe^{III}(CN)−ES adduct upon addition of a 10-fold molar excess of KCN.

Remarkably, in the absence of a substrate (L-Cys), no cyanide binding could be observed by EPR spectroscopy even following addition of a 100-fold molar excess of cyanide relative to enzyme. This apparent obligate ordered addition of substrate prior to cyanide has also been observed in experiments in which nitric oxide was used as a surrogate for O_2 binding. However, to the best of our knowledge, the obligate-ordered addition of substrate prior to cyanide has not been previously observed for other non-heme mononuclear iron enzymes.

As with the steady-state experiments, the AI-CDO used in these experiments has approximately 50% C93−Y157 cross-link (α) as indicated by SDS−PAGE densitometry. As shown in Figure 7, two spectroscopically distinct $S = {}^1/_2$ species can be observed in AI Fe^{III}(CN)−ES samples. As indicated by Figure 7, one of the $S = {}^1/_2$ species has g-values identical to those observed in samples of the CN/Cys-bound Fe^{III}−α-CDO complex (**S1**). However, an additional $S = {}^1/_2$ signal (**S2**) can be observed with g-values of 2.34, 2.21, and 1.95. The individual contribution of each species in the observed spectra was determined by quantitative simulation [**S1** (60%) and **S2** (40%) (dashed line)] and least-squares fitting. Because **S2** is observed only when it is prepared from AI-CDO, it is likely that this signal originates from the β fraction of the Fe^{III}−AI-CDO complex lacking the covalently cross-linked C93−Y157 pair (β-CDO). While the fraction of **S1** and **S2** analytically determined by quantitative simulation slightly differs from the expected values obtained by SDS−PAGE, the values obtained are well within the error associated with gel densitometry. As additional confirmation of this assignment, samples of CN/Cys-bound Fe^{III}−CDO were prepared from the C93A variant. As indicated in Figure 7, only one low-spin ferric signal is observed with g-values (2.35, 2.22, and 1.94) nearly identical to those observed for **S2**. Additionally, the half-power microwave saturation at 10 K for the C93A CN/Cys-bound Fe^{III}−CDO complex is essentially equivalent to that observed for α-CDO ($P_{1/2} = 160$ μW; $b = 1.0$).

dx.doi.org/10.1021/bi4010232 | Biochemistry 2013, 52, 9104−9119

Table 2. Simulation Parameters for the L-Cys-Bound, D-Cys-Bound, and L-Sec (CN/substrate)-Bound ($S = {}^1/_2$) Fe^{III}–CDO Samples[a]

species	g_1	g_2	g_3	σg_1	σg_2	σg_3
S1 (α)	1.937	2.234	2.379	0.001	0.007	0.010
S2 (β)	1.951	2.208	2.343	0.023	0.010	0.010
α-Fe^{III}(CN/L-Cys)	1.937	2.234	2.379	0.001	0.007	0.010
α-Fe^{III}(CN/D-Cys)	1.932	2.243	2.384	0.015	0.015	0.023
α-Fe^{III}(CN/L-Sec)	1.959	2.262	2.446	0.012	0.004	0.019

[a]All simulations utilize a minimal line width (σ_B) of 0.9 mT.

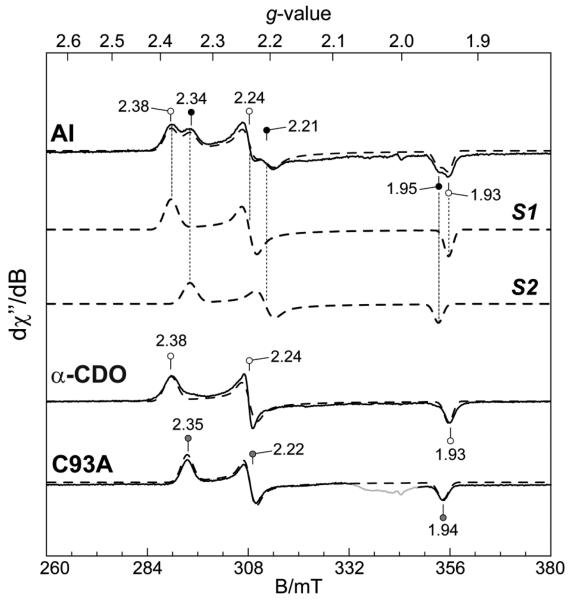

Figure 7. X-Band EPR spectra of the CN/Cys-bound Fe^{III}–CDO complex prepared from as-isolated (AI), fully modified (α-CDO), and C93A CDO enzymes. EPR spectroscopic simulations (– – –) of **S1** and **S2** are overlaid on the spectra (—) for comparison. The component simulation to AI spectra is produced by two spectroscopically distinct low-spin ferric ($S = {}^1/_2$) sites. Instrumental parameters: microwave frequency, 9.64 GHz; modulation frequency, 100 kHz; modulation amplitude, 0.9 mT; temperature, 10 K; microwave power, 6 μW (45 dB). Simulation parameters are listed in Table 2.

Interestingly, CDO variants Y157F and H155A, which exhibit no or vastly diminished catalytic activity, were also unable to bind cyanide in the substrate-bound Fe^{III} oxidation state. Indeed, even at excess cyanide concentrations (100-fold molar excess, 15 mM) no low-spin ferric signals could be detected. Thus, on the basis of these experiments, the catalytic activity of CDO can be correlated to the ability of the substrate-bound enzyme to bind cyanide.

While it was originally developed for the study of heme metalloproteins and complexes, it is frequently useful to use the model initially developed by Griffith[65] to analyze the EPR spectra of low-spin ferric complexes. This model assumes that the ligand field splitting separating the t_{2g} and e_g orbitals is significantly large to prevent orbital mixing. By neglecting the influence of the unoccupied e_g orbitals, a simplified model can be envisioned in which the tetragonal (Δ/λ) and rhombic (V/Δ) components of the t_{2g} orbital splitting can be determined from the experimentally observed g-values.[66] (In this context, Δ refers to the tetragonal ligand field strength and not the zero-field splitting of a non-Kramers doublet.) Equations 5 and 6 show the relationships developed by Taylor for the determination of V, Δ, on the basis of the observed g-values (g_1–g_3), and the one-electron spin–orbit coupling constant (λ_{Fe}).[66−68]

$$\frac{V}{\lambda_{Fe}} = \frac{g_x}{g_x + g_y} + \frac{g_y}{g_z - g_x} \quad (5)$$

$$\frac{\Delta}{\lambda_{Fe}} = \frac{g_x}{g_z + g_y} + \frac{g_z}{g_y - g_x} - \frac{V}{2\lambda_{Fe}} \quad (6)$$

For low-spin ferric complexes, λ_{Fe} is typically ~400 cm^{-1}.[67−69] An additional term (k), the "orbital reduction factor", can be determined from the observed g-values to account for covalency. For low-spin heme centers, the value of k is typically <1.0.[70] However, in instances in which $k \geq 1$, for example, some non-heme iron centers, the assumption that the excited e_g orbitals do not interact with the ground t_{2g} set is not fully justified.[67,69,71]

Table 3. EPR and Calculated Ligand Field Parameters Observed for Low-Spin Non-Heme Ferric Iron Centers

protein[a]	g_1	g_2	g_3	Δ/λ	V/Δ	k	ref
Fe^{III}(CN/Cys) (α-CDO)	1.94	2.23	2.38	5.65	0.98	1.15	this work
Fe^{III}(CN/Cys) (β-CDO)	1.95	2.21	2.34	6.53	0.93	1.17	this work
Fe^{III}(CN/Sec) (α-CDO)	1.96	2.26	2.45	5.89	0.87	1.26	this work
Fe^{III}(CN/Sec) (β-CDO)	1.94	2.24	2.38	5.56	1.00	1.20	this work
Fe^{III}(CN/Cys) C93A	1.94	2.22	2.35	6.14	0.98	1.19	this work
Fe^{III}(CN)–SOR	1.97	2.13	2.27	10.8	0.70	1.00	68
Fe^{III}–NH	1.92	2.18	2.45	7.55	0.61	1.14	69
Fe^{III}(CN)–AK	1.89	2.21	2.43	5.72	0.80	1.11	77
$Fe^{III}(CN)_2$–PCD	1.90	2.18	2.41	6.65	0.71	1.00	78
Fe^{III}–BLM	1.94	2.17	2.26	6.64	1.09	0.92	79
activated BLM	1.94	2.23	2.38	5.65	0.98	0.82	79

[a]Abbreviations: SOR, superoxide reductase; NH, nitrile hydratase; AK, adenylate kinase; PCD, protocatechuate 3,4-dioxygenase; BLM, bleomycin.

dx.doi.org/10.1021/bi4010232 | Biochemistry 2013, 52, 9104−9119

On the basis of the *g*-values obtained from **S2**, a tetragonal splitting (Δ/λ = 6.53) is obtained for the ternary complex in the absence of the C93−Y157 pair. Alternatively, in samples prepared from α-CDO (**S1**), a decrease in the tetragonal splitting (Δ/λ = 5.65) is observed. However, both **S1** and **S2** exhibit very similar rhombic distortion (V/Δ values of 0.98 and 0.93, respectively). These findings indicate that the C93−Y157 pair decreases the magnitude of the low-spin ferric iron tetragonal field (Δ) without significantly altering the rhombicitiy (V/Δ) of the CN/Cys-bound Fe^{III} site. As expected, the tetragonal splitting and rhombic distortion for the C93A CN/Cys-bound Fe^{III}−CDO complex are comparable to the values obtained for **S2** (for C93A, Δ/λ = 6.14 and V/Δ = 0.98). This observation suggests that the decreased tetragonal distortion in the presence of the C93−Y157 pair can mainly be attributed to a decrease in the level of cyano−ligand π-backbonding.

Alternatively, in samples of the Fe^{III}−CDO species bound by L-selenocysteine (L-Sec), the presence of the C93−Y157 pair has an only modest impact on the tetragonal splitting (Δ/λ) of the ternary complex (5.89 and 5.56 for α- and β-CDO, respectively). However, a more significant difference can be observed in the rhombic distortion [V/Δ = 0.87 (α) and 1.00 (β)]. These observations suggest that for the L-Sec-bound ternary complexes, the presence of the C93−Y157 pair alters both cyano backbonding and substrate coordination geometry. For comparison, the observed *g*, Δ/λ, and V/Δ values for selected low-spin non-heme iron centers are listed in Table 3.

The alignment of the **g**-tensor trace (g_1−g_3) relative to the molecular axes can be qualitatively interrogated to develop greater insight into the role of these second-sphere interactions within the enzymatic active site. As illustrated in Figure 8, samples of the CN/Cys-bound Fe^{III}-α-CDO complex were prepared utilizing L-Cys (top) and D-Cys (middle). Not surprisingly, the *g*-values observed for each ternary complex are essentially identical as determined by quantitative simulation (listed in Table 2). This suggests that substitution of D-Cys for L-Cys does not significantly alter the electronic structure of the CN/Cys-bound Fe^{III} site. However, the line width observed for samples prepared from D-Cys is significantly broader than those prepared from L-Cys. As stated previously, the spectral line width for these signals is dominated by distributions in the observed *g*-values (*g* strain). As shown in Table 2, samples of the CN/Cys-bound Fe^{III}−CDO complex prepared from D-Cys exhibit significantly greater *g* strain (σg_1 = 0.015, σg_2 = 0.015, and σg_3 = 0.023) than samples prepared from L-Cys (σg_1 = 0.001, σg_2 = 0.007, and σg_3 = 0.010). Analogous to the Debye−Waller factors (*B* factors) reported via crystallography, the increased *g* strain observed for binding of D-Cys to the Fe^{III} site indicates greater coordination lability within the active site relative to that with L-Cys. Interestingly, this increase in *g* strain is significantly more pronounced (15-fold) along the g_1 axis (1.93) than along the g_2 and g_3 axes (2.1- and 2.3-fold, respectively). By inspection of the enzyme−substrate complex (Figure 1), it is reasonable to conclude that altering the stereochemistry of the substrate Cys from L to D would disrupt any stabilizing interactions with the hydroxyl group of the C93−Y157 pair. As the Cys amine group is directly adjacent to the substrate carboxylate group, altering the substrate chiral center is expected to have the greatest influence on the stability of Fe−amine coordination. This observation implies that the g_1 axis of the CN/Cys-bound Fe site is closely associated with the Fe−$N_{(Cys)}$ bond.

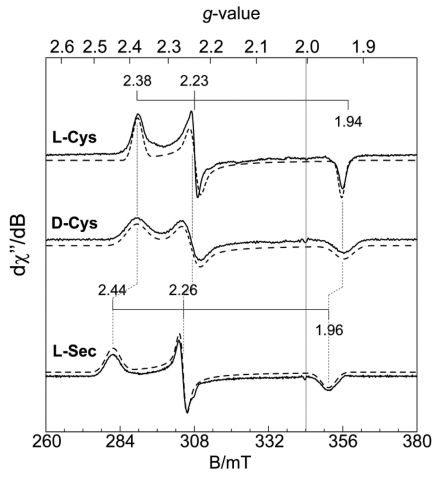

Figure 8. X-Band EPR spectra of L-Cys, D-Cys, and L-Sec CN/substrate-bound Fe^{III}−CDO complexes prepared from α-CDO. EPR spectroscopic simulations (−−−) are overlaid on the spectra (—) for comparison. Instrumental parameters: microwave frequency, 9.64 GHz; modulation frequency, 100 kHz; modulation amplitude, 0.9 mT; temperature, 10 K; microwave power, 6 μW (45 dB). Simulations parameters for $S = {}^1/_2$ species are listed in Table 3.

While CDO cannot utilize L-Sec as a substrate, for the purposes of providing an additional reference point in relating the observed *g*-values to a molecular coordinate system, it is instructive to prepare samples of CN/Sec-bound Fe^{III}−α-CDO for comparison. As indicated in Figure 8 (simulation parameters listed in Table 2), samples prepared by substituting L-Sec for L-Cys also exhibit a rhombic $S = {}^1/_2$ EPR spectrum. Not surprisingly, the *g*-values observed for L-Sec (2.44, 2.26, and 1.96) are shifted slightly relative to those of L-Cys; however, this is most pronounced along the g_3 axis ($\Delta g \sim 0.08$) relative to the g_2 or g_1 axis (Δg value of ∼0.03 or ∼0.02, respectively). This observation suggests that the g_3 axis is correlated to the Fe−$S_{(Cys)}$ bond. Indeed, the increased polarizability of the sulfur atom within the Fe−$S_{(Cys)}$ bond should exhibit significantly greater spin−orbit coupling than other Fe-coordinating atoms. Therefore, it is expected that this bond also gives rise to the largest deviation between the observed *g* value and the electron *g* factor ($g_e \sim 2.0023$). Finally as the g_1, g_2, and g_3 axes must be mutually orthogonal, if g_1 and g_3 are assigned correctly, it is reasonable to conclude that the g_2 axis roughly corresponds to the Fe−CN bond. It should be noted that, although the proposed *g* axis assignments are consistent with spectroscopic observables provided above, this simplistic interpretation implies that the **g**-tensor is essentially colinear with the pseudo-octrahedral symmetry of the CN/Cys-bound Fe^{III} site ligand coordination. However, additional DFT calculations (discussed below) are necessary to analytically verify the orientation of the **g**-tensor with respect to the Fe^{III} site molecular axis system and provide additional insight into the effect of the C93−Y157 cross-link on the electronic structure of the ternary complex.

QM/MM Computational Models of the CN/Cys-Bound Fe^{III}−CDO Active Site. The EPR spectra of the two isoforms of CDO complexed with either L-Cys or L-Sec and cyanide were used to validate the QM/MM-optimized geometries of these species. Both the predicted and experimentally observed *g*-values for these species are listed in Table 4. Although our computational results only partially reproduce the large *g*

dx.doi.org/10.1021/bi4010232 | *Biochemistry* 2013, 52, 9104−9119

Table 4. Experimentally Determined and Computationally Predicted *g*-values for the Species Discussed in This Work

species	non-cross-linked (β)			cross-linked (α)		
	g_1	g_2	g_3	g_1	g_2	g_3
Fe^{III}(CN/Cys), observed	1.951	2.207	2.344	1.937	2.235	2.379
Fe^{III}(CN/Cys), PBE0	2.016	2.155	2.165	2.011	2.167	2.183
Fe^{III}(CN/Cys), B3LYP	2.025	2.135	2.146	2.024	2.145	2.163
Fe^{III}(CN/Sec), observed	1.947	2.236	2.377	1.936	2.254	2.445
Fe^{III}(CN/Sec), PBE0	2.059	2.174	2.182	2.042	2.178	2.198
Fe^{III}(CN/Sec), B3LYP	2.085	2.161	2.181	2.088	2.157	2.183

spread observed experimentally, they properly predict a rhombic EPR spectrum with both functionals tested. This apparent discrepancy may be at least partially ascribed to the nature of the approximations inherent in the CP-SCF calculation used to calculate EPR parameters, which has a known bias for underestimating *g* shifts for complexes containing a first-row transition metal.[72] Although the magnitude of error in our calculated versus experimentally observed *g*-values is larger than what has been previously seen with a set of small test molecules, an increase in the rhombicity for the α-CDO species as compared to that of the non-cross-linked version is both computationally predicted and experimentally observed. Additional validation of computational models may be derived by inspection of the calculated **g**-tensor orientation relative to the molecular coordinate system. Although the **g**-tensor axes obtained from calculations are not strictly colinear with the molecular axes, there is a close correspondence between the two coordinate systems. As indicated by Figure 9, for both isoforms of CDO (α- and β-CDO), DFT calculations predict that the g_1, g_2, and g_3 axes are approximately aligned along the Fe−$N_{(Cys)}$, Fe−$C_{(CN)}$, and Fe−$S_{(Cys)}$ bond axes, respectively. Thus, the computationally derived orientation of the **g**-tensor agrees well with the qualitatively inferred **g** orientation obtained by comparison of the L-Cys, D-Cys, and L-Sec CN/substrate-bound Fe^{III}−CDO EPR signals shown in Figure 8. As the QM/MM-derived models for the CN/Cys-bound Fe^{III}−CDO complex accurately reflect the change in the observed *g* anisotropy upon formation of the C93−Y157 cross-link and predict the orientation of the **g**-tensor, the molecular orbital descriptions and geometric parameters derived from these models clearly warrant further inspection.

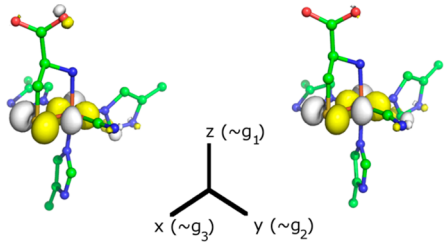

Figure 9. Comparison of the spin down SUMOs of the β (left) and α isoforms (right) of the CN/Cys-bound Fe^{III}−CDO adducts. The approximate orientation of the **g**-tensor, as derived from the computational models, with respect to the molecular axes is also shown.

The CN/Cys adducts of both Fe^{III}-bound α- and β-CDO possess a very similar set of molecular orbitals (MOs) and thus also have the same low-spin Fe(III) ground state as shown in Figure 10. The MOs arising from an Fe−$S_{(Cys)}$ bonding interaction as well as the lone pair on the cysteinyl sulfur are also shown, whereas the Fe−CN and C−N bonding interactions are sufficiently stabilized in energy such that they have been omitted from this figure for the sake of clarity. As expected for a low-spin d^5 ion with approximately octahedral symmetry, the Fe $3d_{xz}$- and $3d_{yz}$-based MOs are doubly occupied, while the $3d_{xy}$-based MO is formally occupied by a single spin up electron. Consequently, it is the electron in this orbital that gives rise to the experimentally observed $S = {}^1/_2$ EPR spectrum. Although it is unoccupied, the spin down Fe $3d_{xy}$-based orbital (the SUMO) provides an excellent representation of the EPR-active orbital, as the composition of the SOMO becomes highly mixed because of spin polarization-induced orbital mixing of the SOMO with the other spin up orbitals.[73] For both the α- and β-CDO adducts, the SUMO contains a significant π^* interaction between the Fe $3d_{xy}$ orbital (~65% of the electron density for this MO) and the sulfur $3p_y$ orbital (~15%) but lacks any sizable contributions from the cyano ligand (<5%). Although the formally singly occupied molecular orbital has little electron density on the cyano group, it is important to note that spin−orbit coupling-induced orbital mixing provides a route by which the nature of

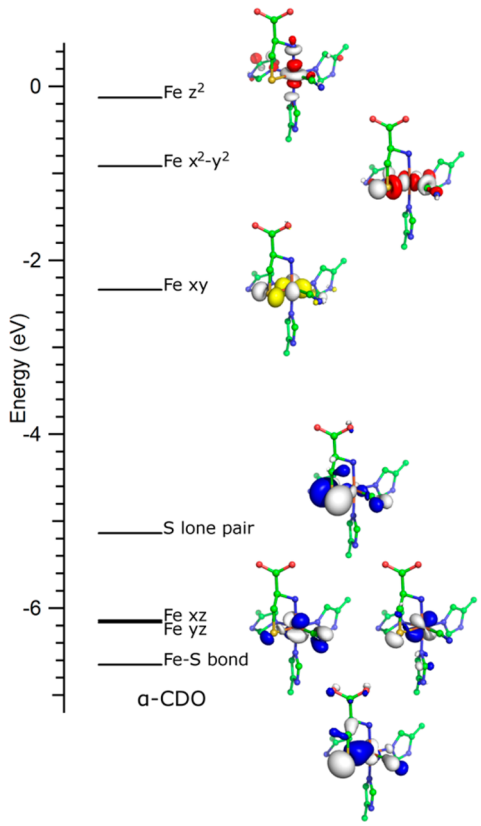

Figure 10. Partial molecular orbital diagram for the α isoform of the CN/Cys-bound Fe^{III}−CDO adduct. For the sake of clarity, hydrogen atoms have been omitted and only the spin down orbitals are shown. Doubly occupied, singly occupied, and unoccupied MOs are colored blue, yellow, and red, respectively.

dx.doi.org/10.1021/bi4010232 | *Biochemistry* 2013, 52, 9104−9119

Table 5. Relevant Bond Lengths (in angstroms) and Angles (in degrees) of the QM/MM-Optimized Active Sites

species[a]	Fe−$S_{(Cys)}$/$Se_{(Sec)}$	Fe−$N_{(Cys/Sec)}$	Fe−$C_{(CN)}$−$N_{(CN)}$	His86−Fe−$C_{(CN)}$
Fe^{III}(CN/Cys)-α	2.28	2.09	169.2	168.6
Fe^{III}(CN/Cys)-β	2.26	2.11	176.3	172.6
Fe^{III}(CN/Sec)-α	2.43	2.10	170.5	167.7
Fe^{III}(CN/Sec)-β	2.41	2.12	176.5	171.9

[a]As defined previously, the cross-linked CDO and non-cross-linked CDO are designated α and β, respectively.

the Fe−CN bond can be probed. The orbitals comprising the e_g set in the parent octahedral symmetry (i.e., the Fe $3d_{x^2-y^2}$ and $3d_{z^2}$ orbitals) are unoccupied and have an energy much higher than that of the t_{2g} set of Fe-based orbitals.

Judging by the QM/MM-optimized geometries of the α and β forms of CDO complexed with L-Cys and cyanide, the three-His facial triad motif is not perturbed upon formation of the C93−Y157 cross-link, with bond lengths and angles that are very similar between the two species (see Table 5). Similarly, the Fe−C and cyanide C−N bond distances are invariant between the two forms of CDO. However, as illustrated in Figure 11, the orientation of the cyanide ligand and the carboxylic acid group on the bound L-Cys are very sensitive to the second-sphere cross-link, with the Fe−C−N unit being considerably more linear when the cross-link is absent. This arrangement moves the nitrogen of the cyano group near the H_δ atom of the highly conserved H155 residue, such that these atoms come to lie within the sum of their van der Waals radii. Additionally, a network of hydrogen bonds exists such that both the guanidyl group of R60 and the phenol of Y157 interact with one of the carboxylic acid oxygens on the bound L-Cys. Conversely, the formation of the covalent C93−Y157 bond moves the Y157 phenol group away from the side chain of R60, in turn pulling the carboxylic acid group of the substrate into a position that allows both of its oxygens to interact with an amide hydrogen on R60's guanidyl group (see Figure 11). Together, these computational results suggest that both the phenol group on Y157 and the guanidyl group of R60 play a major role in the recognition of the Cys substrate, while H155 may play a role in O_2 recognition.

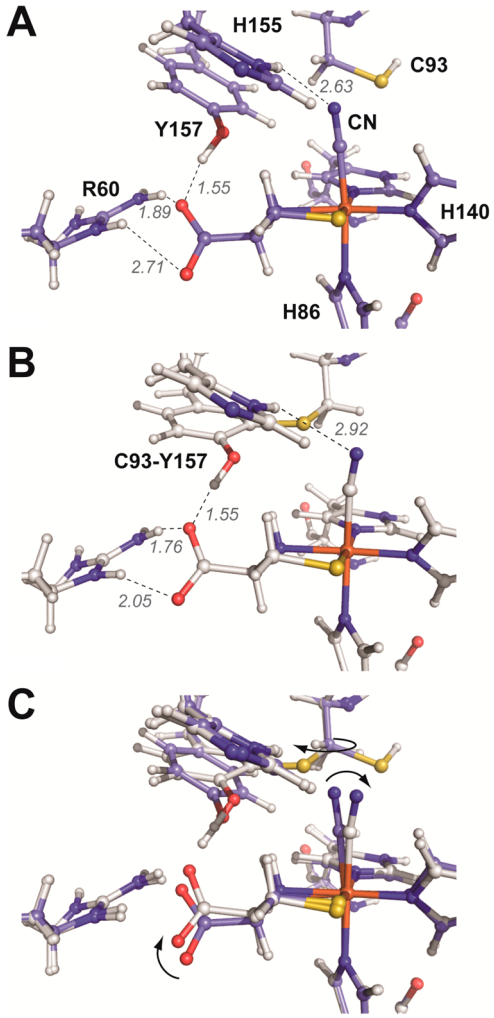

Figure 11. QM/MM-optimized structures of non-cross-linked (A) and cross-linked (B) CN/Cys-bound Fe^{III}−CDO adducts. An overlay of both structures is shown in panel C. Selected distances indicated by the dashed lines are given in angstroms. Arrows in panel C represent major structural changes within the CN/Cys-bound Fe^{III}−CDO site upon formation of the C93−Y157 cross-link.

DISCUSSION

The ability of substrate-bound CDO to bind exogenous ligands in both the Fe^{II} and Fe^{III} oxidation states supports an inner-sphere model for O_2 activation. Historically, azido, carbonyl, and cyano ligands have been employed as a means of spectroscopically characterizing noncovalent interactions (distal effects) between the coordinated ligand and the solvent or protein environment in heme oxygenase enzymes.[74] However, while key second-sphere residues have been identified in non-heme mononuclear iron enzymes, fewer spectroscopic studies are available for comparison.[40]

Consistent with previous reports, the vast difference observed between the rate of α-CDO product formation and those of AI-CDO and the C93A variant clearly demonstrates that formation of the C93−Y157 thioether cross-link is an important "activating" event in the maturation of CDO.[37,38] In light of the EPR spectroscopy and QM/MM models that have been generated, the stark difference observed in the steady-state CSA/O_2 coupling efficiency among L-Cys (81%), D-Cys (4%), and CSH (6%) indicates that the C93−Y157 pair is critical for substrate recognition and stabilization of the ES complex and may also help gate access of solvent molecules to the active site following O_2 activation. As the C93A variant exhibits a coupling efficiency (45%) significantly higher than that of the wild-type enzyme utilizing D-Cys, it is clear that the hydroxyl group of Y157 represents a key enzyme−substrate interaction point. This is clearly evident upon comparison of the EPR spectra of L- and D-Cys CN/Cys-bound Fe^{III}−CDO sites. As both species exhibit equivalent g-values, the geometry of the first coordination sphere is essentially unperturbed. However, the increased g strain observed upon disrupting the interaction between C93−Y157 and the Cys carboxylate group indicates a significant increase in the lability of the enzyme−substrate complex. As this effect is most pronounced along the Fe−$N_{(Cys)}$ bond (g_1 axis), we can conclude that one function of the C93−

dx.doi.org/10.1021/bi4010232 | Biochemistry 2013, 52, 9104−9119

Y157 pair is to position the substrate within the active site by securing the Fe−amine coordination. This may also explain the lack of enzymatic activity (and lack of cyanide binding) observed for the Y157F variant despite the ability of the enzyme to stabilize ferrous iron. The cross-link formed between C93 and Y157 also provides structural rigidity to the cross-linked pair, forcing a single conformation of the Y157 residue relative to the substrate-bound active site. The van der Waals radius of the C93−Y157 pair S atom may also add steric bulk to the O_2-binding pocket, thereby shielding the Fe active site from solvent access and resulting in the increased enzymatic coupling efficiency. This would also explain the apparent substrate inhibition behavior exhibited by the C93A variant and when utilizing D-Cys as the substrate in wild-type CDO assays. Moreover, the added bulk of the S atom also forces the Fe−C−N angle (169°) away from its nearly linear (176°) geometry observed in the absence of the C93−Y157 pair. This bend in the Fe−cyano coordination forces the cyano ligand 0.16 Å closer to the substrate thiol S atom. This effect would potentially be more pronounced for π-donating ligands (O_2 and NO), which favor a bent coordination geometry.

The use of cyanide as a spectroscopic probe over nitric oxide offers significant advantages with respect to g spread, sensitivity to Fe coordination angle, and the lack of "EPR active" contaminating species. Prior to the addition of cyanide, the substrate-bound AI-CDO and Fe^{III}−α-CDO (Fe^{III}−ES) cannot be distinguished by EPR spectroscopy. Therefore, no conclusions can be made regarding interactions between bound solvent molecules and the C93−Y157 pair. However, upon addition of cyanide to samples of AI Fe^{III}−ES, two $S = {}^1/_2$ signals (**S1** and **S2**) are observed. Alternatively, addition of cyanide to the substrate-bound Fe^{III}−α-CDO adduct yields only one signal (**S1**). As the Fe−C−N angle strongly influences the strength of π-backbonding, cyanide is an ideal probe for monitoring perturbations to the coordination geometry. The decreased tetragonal ligand field strength (Δ/λ) observed for **S1** indicates weaker π-backbonding of the Fe^{III}-bound cyanide ligand than of the non-cross-linked enzyme (**S2**). This correlates well with our QM/MM-optimized geometries, in which the C93−Y157 pair induces a more bent Fe−C−N geometry, resulting in a decreased level of orbital overlap between the Fe 3d- and cyanide π^*-based orbitals. Assuming a reasonable estimate for λ_{Fe} (~400 cm^{-1}),[67−69] the tetragonal field splitting of CDO in the presence of the C93−Y157 thioether cross-link (α-CDO) is ~2260 cm^{-1}. Alternatively, in the absence of the C93−Y157 pair (**S2**; β-CDO), the axial field strength increases to ~2610 cm^{-1} ($\Delta \sim 2500$ cm^{-1} for the C93A variant). Thus, the deviation in axial field strength (350 cm^{-1}) between α- and β-CDO corresponds to ~4.2 kJ/mol, approximately equivalent to the strength of a weak hydrogen bond.

As the H155A and Y157F variants are completely unable to bind cyanide, the role of second-sphere interactions with the substrate-bound active site cannot be confirmed by EPR spectroscopy. However, the vastly decreased activity or complete inactivity of these CDO variants suggests that these residues represent another key second-sphere interaction relevant to catalysis. The QM/MM models provided here suggest that this residue could serve as a stabilizing hydrogen bonding interaction with bound Fe−oxo intermediates during native catalysis, similar to H200 of 2,3-dioxygenase.[39] However, further experiments are necessary to verify this hypothesis.

In summary, the results provided here suggest that the C93−Y157 post-translational modification is critical for efficient enzymatic coupling. Coupling assays with substrate analogues (D-Cys and CSH) suggest that the hydroxyl group of Y157 represents a key point enzyme−substrate interaction necessary for efficient oxidative coupling. Additionally, the computational models presented here provide a reasonable explanation for the differences observed in both enzymatic activity and spectroscopic observables between the cross-linked and non-cross-linked enzyme. While both spectroscopic measurements and computational models were performed on the catalytically inactive CN/Cys-bound Fe^{III}−CDO state, the pronounced decrease in k_{cat} and CSA/O_2 coupling efficiency observed by altering the interactions between the Y157 hydroxyl and R60 guanidyl groups with the substrate Cys carboxyl group clearly demonstrates the relevance of these interactions in native catalysis. The obligate ordered addition of substrate prior to cyanide observed in samples of the Fe^{III}−CDO adduct is consistent with experiments utilizing nitric oxide as a spectroscopic probe for O_2 binding.[43] However, to the best of our knowledge, this has not previously been observed for other non-heme iron oxidase or oxygenase enzymes in experiments utilizing cyanide. This result is particularly intriguing in light of the prevailing theories proposed to explain the substrate-gated O_2 regulation exhibited by non-heme mononuclear iron enzymes: (1) thermodynamic gating of the Fe^{II}/Fe^{III} redox couple upon substrate binding and (2) Fe site conformational changes that facilitate direct O_2 coordination.[20,75,76] Compared to that of nitric oxide, the binding of cyanide should be less influenced by the reduction potential of the active site, suggesting that thermodynamic gating cannot be solely responsible for regulating O_2 activation in CDO.

■ ASSOCIATED CONTENT

Supporting Information

Parallel mode X-band EPR spectra of the resting Fe^{II}−CDO adduct, partial molecular orbital diagrams, and converged active site coordinates for the α and β isoforms of CN/Cys-bound CDO. This material is available free of charge via the Internet at http://pubs.acs.org.

■ AUTHOR INFORMATION

Corresponding Author

*Department of Chemistry and Biochemistry, 700 Planetarium Pl., Room 130, The University of Texas at Arlington, Arlington, TX 76019. E-mail: bspierce@uta.edu. Phone: (817) 272-9066. Fax: (817) 272-3808.

Funding

This work was supported by National Science Foundation (NSF) Grant (CHE)1213655 (B.S.P.) and by NSF Grant (CHE)0840494 (computational resources).

Notes

The authors declare no competing financial interest.

■ ACKNOWLEDGMENTS

We thank The University of Texas at Arlington Center for Nanostructured Materials for the use of EPR instrumentation.

■ ABBREVIATIONS

CDO, cysteine dioxygenase; CSH, 2-aminoethanethiol (cysteamine); CSA, cysteinesulfinic acid; Sec, selenocysteine; HPLC, high-performance liquid chromatography; Ni-IMAC, immobi-

lized metal (Ni) affinity chromatography; EPR, electron paramagnetic resonance; ROS, reactive oxygen species; DFT, density functional theory; QM/MM, quantum mechanics/molecular mechanics; MO, molecular orbital.

REFERENCES

(1) Reddie, K. G., and Carroll, K. S. (2008) Expanding the functional diversity of proteins through cysteine oxidation. *Curr. Opin. Chem. Biol. 12*, 746−754.

(2) Winyard, P. G., Moody, C. J., and Jacob, C. (2005) Oxidative activation of antioxidant defence. *Trends Biochem. Sci. 30*, 453−461.

(3) Trachootham, D., Alexandre, J., and Huang, P. (2009) Targeting cancer cells by ROS-mediated mechanisms: A radical therapeutic approach? *Nat. Rev. Drug Discovery 8*, 579−591.

(4) Behave, D. P., Muse, W. B., and Carroll, K. S. (2007) Drug Targets in Mycobacterial Sulfur Metabolism. *Infect. Disord.: Drug Targets 7*, 140−158.

(5) Deth, R., Muratore, C., Benzecry, J., Power-Charnitsky, V.-A., and Waly, M. (2008) How environmental and genetic factors combine to cause autism: A redox/methylation hypothesis. *NeuroToxicology 29*, 190−201.

(6) James, S. J., Cutler, P., Melnyk, S., Jernigan, S., Janak, L., Gaylor, D. W., and Neubrander, J. A. (2004) Metabolic biomarkers of increased oxidative stress and impaired methylation capacity in children with autism. *Am. J. Clin. Nutr. 80*, 1611−1617.

(7) Gordon, C., Emery, P., Bradley, H., and Waring, H. (1992) Abnormal sulfur oxidation in systemic lupus erythematosus. *Lancet 229*, 25−26.

(8) Simmons, C. R., Hirschberger, L. L., Machi, M. S., and Stipanuk, M. H. (2006) Expression, purification, and kinetic characterization of recombinant rat cysteine dioxygenase, a non-heme metalloenzyme necessary for regulation of cellular cysteine. *Protein Expression Purif. 47*, 74−81.

(9) Heafield, M. T., Fearn, S., Steventon, G. B., Waring, R. H., Williams, A. C., and Sturman, S. G. (1990) Plasma cysteine and sulfate levels in patients with motor neurone, Parkinson's and Alzheimer's disease. *Neurosci. Lett. 110*, 216−220.

(10) Dominy, J. E., Jr., Simmons, C. R., Karplus, P. A., Gehring, A. M., and Stipanuk, M. H. (2006) Identification and Characterization of Bacterial Cysteine Dioxygenases: A New Route of Cysteine Degradation for Eubacteria. *J. Bacteriol. 188*, 5561−5569.

(11) Stipanuk, M., Simmons, C., Andrew Karplus, P., and Dominy, J. (2010) Thiol dioxygenases: Unique families of cupin proteins. *Amino Acids 41*, 1−12.

(12) Chai, S. C., Jerkins, A. A., Banik, J. J., Shalev, I., Pinkham, J. L., Uden, P. C., and Maroney, M. J. (2005) Heterlogous Expression, Purification, and Characterization of Recombinant Rat Cysteine Dioxygenase. *J. Biol. Chem. 280*, 9865−9869.

(13) Bagley, P. J., Hirschberger, L. L., and Stipanuk, M. H. (1995) Evaluation and Modification of an Assay Procedure for Cysteine Dioxygenase Activity: High-Performance Liquid Chromatography Method for Measurement of Cysteine Sulfinate and Demonstration of Physiological Relevance of Cysteine Dioxygenase Activity in Cysteine Catabolism. *Anal. Biochem. 227*, 40−48.

(14) McCoy, J. G., Bailey, L. J., Bitto, E., Bingman, C. A., Aceti, D. J., Fox, B. G., and Phillips, G. N., Jr. (2006) Structure and mechanism of mouse cysteine dioxygenase. *Proc. Natl. Acad. Sci. U.S.A. 103*, 3084−3089.

(15) Ye, S., Wu, X. a., Wei, L., Tang, D., Sun, P., Bartlam, M., and Rao, Z. (2007) An Insight into the Mechanism of Human Cysteine Dioxygenase: Key Roles of the Thioether-Bonded Tyrosine-Cysteine Cofactor. *J. Biol. Chem. 282*, 3391−3402.

(16) Straganz, G. D., and Nidetzky, B. (2006) Variations of the 2-His-1-carboxylate Theme in Mononuclear Non-Heme Fe(II) Enzymes. *ChemBioChem 7*, 1536−1548.

(17) Straganz, G. D., Diebold, A. R., Egger, S., Nidetzky, B., and Solomon, E. I. (2010) Kinetic and CD/MCD Spectroscopic Studies of the Atypical, Three-His-Ligated, Non-Heme Fe^{2+} Center in Diketone Dioxygenase: The Role of Hydrophilic Outer Shell Residues in Catalysis. *Biochemistry 49*, 996−1004.

(18) Adams, M. A., Singh, V. K., Keller, B. O., and Jia, Z. (2006) Structural and biochemical characterization of gentisate 1,2-dioxygenase from *Escherichia coli* O157:H7. *Mol. Microbiol. 61*, 1469−1484.

(19) Dominy, J. E., Simmons, C. R., Hirschberger, L. L., Hwang, J., Coloso, R. M., and Stipanuk, M. H. (2007) Discovery and Characterization of a Second Mammalian Thiol Dioxygenase, Cysteamine Dioxygenase. *J. Biol. Chem. 282*, 25189−25198.

(20) Solomon, E. I., Decker, A., and Lehnert, N. (2003) Non-heme iron enzymes: Contrasts to heme catalysis. *Proc. Natl. Acad. Sci. U.S.A. 100*, 3589−3594.

(21) Krebs, C., Galonić Fujimori, D., Walsh, C. T., and Bollinger, J. M. (2007) Non-Heme Fe(IV)−Oxo Intermediates. *Acc. Chem. Res. 40*, 484−492.

(22) Kurtz, D. M. J. (2006) Avoiding high-valent iron intermediates: Superoxide reductase and rubrerythrin. *J. Inorg. Biochem. 100*, 679−693.

(23) Matthews, M. L., Krest, C. M., Barr, E. W., Vaillancourt, F. d. r. H., Walsh, C. T., Green, M. T., Krebs, C., and Bollinger, J. M. (2009) Substrate-Triggered Formation and Remarkable Stability of the C−H Bond-Cleaving Chloroferryl Intermediate in the Aliphatic Halogenase, SyrB2. *Biochemistry 48*, 4331−4343.

(24) Makris, T. M., Chakrabarti, M., Münck, E., and Lipscomb, J. D. (2010) A family of diiron monooxygenases catalyzing amino acid β-hydroxylation in antibiotic biosynthesis. *Proc. Natl. Acad. Sci. U.S.A. 107*, 15391−15396.

(25) Brown, C. D., Neidig, M. L., Neibergall, M. B., Lipscomb, J. D., and Solomon, E. I. (2007) VTVH-MCD and DFT Studies of Thiolate Bonding to $\{FeNO\}^7/\{FeO2\}^8$ Complexes of Isopenicillin N Synthase: Substrate Determination of Oxidase versus Oxygenase Activity in Nonheme Fe Enzymes. *J. Am. Chem. Soc. 129*, 7427−7438.

(26) Blasiak, L. C., and Drennan, C. L. (2009) Structural Perspective on Enzymatic Halogenation. *Acc. Chem. Res. 42*, 147−155.

(27) Vaillancourt, F. H., Yeh, E., Vosburg, D. A., Garneau-Tsodikova, S., and Walsh, C. T. (2006) Nature's Inventory of Halogenation Catalysts: Oxidative Strategies Predominate. *Chem. Rev. 106*, 3364−3378.

(28) Ito, N., Phillips, S. E. V., Stevens, C., Ogel, Z. B., McPherson, M. J., Keen, J. N., Yadav, K. D. S., and Knowles, P. F. (1991) Novel thioether bond revealed by a 1.7 Å crystal structure of galactose oxidase. *Nature 350*, 87−90.

(29) Schnell, R., Sandalova, T., Hellman, U., Lindqvist, Y., and Schneider, G. (2005) Siroheme- and [Fe4-S4]-dependent NirA from *Mycobacterium tuberculosis* Is a Sulfite Reductase with a Covalent Cys-Tyr Bond in the Active Site. *J. Biol. Chem. 280*, 27319−27328.

(30) Whittaker, J. W. (2003) Free Radical Catalysis by Galactose Oxidase. *Chem. Rev. 103*, 2347−2363.

(31) Díaz, A., Horjales, E., Rudiño-Piñera, E., Arreola, R., and Hansberg, W. (2004) Unusual Cys-Tyr Covalent Bond in a Large Catalase. *J. Mol. Biol. 342*, 971−985.

(32) Koehntop, K., Marimanikkuppam, S., Ryle, M., Hausinger, R., and Que, L. (2006) Self-hydroxylation of taurine/α-ketoglutarate dioxygenase: Evidence for more than one oxygen activation mechanism. *JBIC, J. Biol. Inorg. Chem. 11*, 63−72.

(33) Ryle, M. J., Koehntop, K. D., Liu, A., Que, L., and Hausinger, R. P. (2003) Interconversion of two oxidized forms of taurine/α-ketoglutarate dioxygenase, a non-heme iron hydroxylase: Evidence for bicarbonate binding. *Proc. Natl. Acad. Sci. U.S.A. 100*, 3790−3795.

(34) Ge, Y., Lawhorn, B. G., El Naggar, M., Sze, S. K., Begley, T. P., and McLafferty, F. W. (2003) Detection of four oxidation sites in viral prolyl-4-hydroxylase by top-down mass spectrometry. *Protein Sci. 12*, 2320−2326.

(35) Farquhar, E. R., Koehntop, K. D., Emerson, J. P., and Que, L., Jr. (2005) Post-translational self-hydroxylation: A probe for oxygen activation mechanisms in non-heme iron enzymes. *Biochem. Biophys. Res. Commun. 338*, 230−239.

(36) Myllylä, R., Majamaa, K., Günzler, V., Hanauske-Abel, H. M., and Kivirikko, K. I. (1984) Ascorbate is consumed stoichiometrically

in the uncoupled reactions catalyzed by prolyl 4-hydroxylase and lysyl hydroxylase. *J. Biol. Chem. 259*, 5403−5405.
(37) Dominy, J. E., Jr., Hwang, J., Guo, S., Hirschberger, L. L., Zhang, S., and Stipanuk, M. H. (2008) Synthesis of Amino Acid Cofactor in Cysteine Dioxygenase Is Regulated by Substrate and Represents a Novel Post-translational Regulation of Activity. *J. Biol. Chem. 283*, 12188−12201.
(38) Siakkou, E., Rutledge, M. T., Wilbanks, S. M., and Jameson, G. N. L. (2011) Correlating crosslink formation with enzymatic activity in cysteine dioxygenase. *Biochim. Biophys. Acta 1814*, 2003−2009.
(39) Mbughuni, M. M., Chakrabarti, M., Hayden, J. A., Bominaar, E. L., Hendrich, M. P., Münck, E., and Lipscomb, J. D. (2010) Trapping and spectroscopic characterization of an Fe^{III}-superoxo intermediate from a nonheme mononuclear iron-containing enzyme. *Proc. Natl. Acad. Sci. U.S.A. 107*, 16788−16793.
(40) Hayden, J., Farquhar, E., Que, L., Lipscomb, J., and Hendrich, M. (2013) NO binding to Mn-substituted homoprotocatechuate 2,3-dioxygenase: Relationship to O_2 reactivity. *JBIC, J. Biol. Inorg. Chem.*, 1−12.
(41) Groce, S. L., and Lipscomb, J. D. (2003) Conversion of Extradiol Aromatic Ring-Cleaving Homoprotocatechuate 2,3-Dioxygenase into an Intradiol Cleaving Enzyme. *J. Am. Chem. Soc. 125*, 11780−11781.
(42) Crawford, J. A., Li, W., and Pierce, B. S. (2011) Single Turnover of Substrate-Bound Ferric Cysteine Dioxygenase with Superoxide Anion: Enzymatic Reactivation, Product Formation, and a Transient Intermediate. *Biochemistry 50*, 10241−10253.
(43) Pierce, B. S., Gardner, J. D., Bailey, L. J., Brunold, T. C., and Fox, B. G. (2007) Characterization of the Nitrosyl Adduct of Substrate-Bound Mouse Cysteine Dioxygenase by Electron Paramagnetic Resonance: Electronic Structure of the Active Site and Mechanistic Implications. *Biochemistry 46*, 8569−8578.
(44) Gardner, J. D., Pierce, B. S., Fox, B. G., and Brunold, T. C. (2010) Spectroscopic and Computational Characterization of Substrate-Bound Mouse Cysteine Dioxygenase: Nature of the Ferrous and Ferric Cysteine Adducts and Mechanistic Implications. *Biochemistry 49*, 6033−6041.
(45) Abragam, A., and Bleaney, B. (1970) *Electron Paramagnetic Resonance of Transition Ions*, International Series of Monographs on Physics, Oxford University Press, Oxford, U.K.
(46) Frisch, M. J., Trucks, G. W., Schlegel, H. B., Scuseria, G. E., Robb, M. A., Cheeseman, J. R., Scalmani, G., Barone, V., Mennucci, B., Petersson, G. A., Nakatsuji, H., Caricato, M., Li, X., Hratchian, H. P., Izmaylov, A. F., Bloino, J., Zheng, G. J. L., Sonnenberg, J. L., Hada, M., Ehara, M., Toyota, K., Fukuda, R., Hasegawa, J., Ishida, M., Nakajima, T., Honda, Y., Kitao, O., Nakai, H., Vreven, T., Montgomery, J. A., Jr., Peralta, J. E., Ogliaro, F., Bearpark, M., Heyd, J. J., Brothers, E., Kudin, K. N., Staroverov, V. N., Keith, T., Kobayashi, R., Normand, J., Raghavachari, K., Rendell, A., Burant, J. C., Iyengar, S. S., Tomasi, J., Cossi, M., Rega, N., Millam, J. M., Klene, M., Knox, J. E., Cross, J. B., Bakken, V., Adamo, C., Jaramillo, J., Gomperts, R., Stratmann, R. E., Yazyev, O., Austin, A. J., Cammi, R., Pomelli, C., Ochterski, J. W., Martin, R. L., Morokuma, K., Zakrzewski, V. G., Voth, G. A., Salvador, P., Dannenberg, J. J., Dapprich, S., Daniels, A. D., Farkas, O., Foresman, J. B., Ortiz, J. V., Cioslowski, J., and Fox, D. J. (2010) *Gaussian 09*, revision C.01, Gaussian, Inc., Wallingford, CT.
(47) Lee, C. T., Yang, W. T., and Parr, R. G. (1988) Development of the Colle-Salvetti Correlation-Energy Formula into a Functional of the Electron-Density. *Phys. Rev. B 37*, 785−789.
(48) Becke, A. D. (1993) Density-Functional Thermochemistry. 3. The Role of Exact Exchange. *J. Chem. Phys. 98*, 5648−5652.
(49) Hehre, W. J., Ditchfie, R., and Pople, J. A. (1972) Self-Consistent Molecular-Orbital Methods. 12. Further Extensions of Gaussian-type Basis Sets for Use in Molecular-Orbital Studies of Organic-Molecules. *J. Chem. Phys. 56*, 2257.
(50) Schafer, A., Horn, H., and Ahlrichs, R. (1992) Fully Optimized Contracted Gaussian-Basis Sets for Atoms Li to Kr. *J. Chem. Phys. 97*, 2571−2577.
(51) Cornell, W. D., Cieplak, P., Bayly, C. I., Gould, I. R., Merz, K. M., Ferguson, D. M., Spellmeyer, D. C., Fox, T., Caldwell, J. W., and Kollman, P. A. (1995) A 2nd Generation Force-Field for the Simulation of Proteins, Nucleic-Acids, and Organic-Molecules. *J. Am. Chem. Soc. 117*, 5179−5197.
(52) Simmons, C. R., Krishnamoorthy, K., Granett, S. L., Schuller, D. J., Dominy, J. E., Begley, T. P., Stipanuk, M. H., and Karplus, P. A. (2008) A Putative Fe^{2+}-Bound Persulfenate Intermediate in Cysteine Dioxygenase. *Biochemistry 47*, 11390−11392.
(53) Word, J. M., Lovell, S. C., Richardson, J. S., and Richardson, D. C. (1999) Asparagine and glutamine: Using hydrogen atom contacts in the choice of side-chain amide orientation. *J. Mol. Biol. 285*, 1735−1747.
(54) Neese, F. (2012) *Orca 2.9.1, An Ab Initio, DFT and Semiempirical Electronic Structure Package*.
(55) *The PyMOL Molecular Graphics System*, version 1.5.0.4, Schrodinger, LLC, Portland, OR.
(56) Adamo, C., and Barone, V. (1999) Toward reliable density functional methods without adjustable parameters: The PBE0 model. *J. Chem. Phys. 110*, 6158−6170.
(57) Kutzelnigg, W., Fleischer, U., and Schindler, M., Eds. (1990) *The IGLO method: Ab initio calculation and interpretation of NMR chemical shifts and magnetic susceptibilities*, Vol. 23, Springer-Verlag, Heidelberg. Germany.
(58) Neese, F. (2002) Prediction and interpretation of the Fe-57 isomer shift in Mossbauer spectra by density functional theory. *Inorg. Chim. Acta 337*, 181−192.
(59) Wachters, A. J. (1970) Gaussian Basis Set for Molecular Wavefunctions Containing Third-Row Atoms. *J. Chem. Phys. 52*, 1033.
(60) Stipanuk, M. H. (2004) Sulfur Amino Acid Metabolism: Pathways for Production and Removal of Homocysteine and Cysteine. *Annu. Rev. Nutr. 24*, 539−577.
(61) Ewetz, L., and Sorbo, B. (1966) Characteristics of the Cysteinesulfinate-Forming Enzyme System in Rat Liver. *Biochim. Biophys. Acta 128*, 296−305.
(62) Sorbo, B., and Ewetz, L. (1965) The Enzymatic Oxidation of Cysteine to Cysteinesulfinate in Rat Liver. *Biochem. Biophys. Res. Commun. 18*, 359−363.
(63) Lombardini, J. B., Singer, T. P., and Boyer, P. D. (1969) Cysteine Oxygenase. *J. Biol. Chem. 244*, 1172−1175.
(64) Hendrich, M. P., and Debrunner, P. G. (1989) Integer-spin electron paramagnetic resonance of iron proteins. *Biophys. J. 56*, 489−506.
(65) Griffith, J. S. (1971) Theory of E.P.R. in low-spin ferric haemoproteins. *Mol. Phys. 21*, 135−139.
(66) Taylor, C. P. S. (1977) The EPR of Low Spin Heme Complexes: Relation of the t_{2g} hole model to the directional properties of the *g*-tensor and a new method for calculating the ligand field parameters. *Biochim. Biophys. Acta 491*, 137−149.
(67) Solomon, E. I., Brunold, T. C., Davis, M. I., Kemsley, J. N., Lee, S.-K., Lehnert, N., Neese, F., Skulan, A. J., Yang, Y.-S., and Zhou, J. (2000) Geometric and Electronic Structure/Function Correlations in Non-Heme Iron Enzymes. *Chem. Rev. 100*, 235−349.
(68) Clay, M. D., Jenney, F. E., Hagedoorn, P. L., George, G. N., Adams, M. W. W., and Johnson, M. K. (2002) Spectroscopic Studies of *Pyrococcus furiosus* Superoxide Reductase: Implications for Active-Site Structures and the Catalytic Mechanism. *J. Am. Chem. Soc. 124*, 788−805.
(69) Popescu, V.-C., Münck, E., Fox, B. G., Sanakis, Y., Cummings, J. G., Turner, I. M., and Nelson, M. J. (2001) Mössbauer and EPR Studies of the Photoactivation of Nitrile Hydratase. *Biochemistry 40*, 7984−7991.
(70) International Conference on Magnetic Resonances in Biological Research, SMCI (1971) *Magnetic resonances in biological research* (Franconi, C., Ed.) Gordon and Breach, New York.
(71) Griffith, J. S. (1971) *The Theory of Transition-Metal Ions*, Cambridge University Press, London.

(72) Neese, F. (2001) Prediction of electron paramagnetic resonance *g* values using coupled perturbed Hartree−Fock and Kohn−Sham theory. *J. Chem. Phys. 115*, 11080−11096.
(73) Seo, D.-K. (2006) Density functional perturbational orbital theory of spin polarization in electronic systems. I. Formalism. *J. Chem. Phys. 125*, 154105.
(74) Sono, M., Roach, M. P., Coulter, E. D., and Dawson, J. H. (1996) Heme-Containing Oxygenases. *Chem. Rev. 96*, 2841−2888.
(75) Solomon, E. I., Brunold, T. C., Davis, M. I., Kemsley, J. N., Lee, S.-K., Lehnert, N., Neese, F., Skulan, A. J., Yang, Y.-S., and Zhou, J. (2000) Geometric and Electronic Structure/Function Correlations in Non-Heme Iron Enzymes. *Chem. Rev. 100*, 235−349.
(76) Costas, M., Mehn, M. P., Jensen, M. P., and Que, L. J. (2004) Dioxygen Activation at Mononuclear Nonheme Iron Active Sites: Enzymes, Models, and Intermediates. *Chem. Rev. 104*, 939−986.
(77) Deligiannakis, Y., Boussac, A., Bottin, H., Perrier, V., Bârzu, O., and Gilles, A.-M. (1997) A New Non-Heme Iron Environment in *Paracoccus denitrificans* Adenylate Kinase Studied by Electron Paramagnetic Resonance and Electron Spin Echo Envelope Modulation Spectroscopy. *Biochemistry 36*, 9446−9452.
(78) Whittaker, J. W., and Lipscomb, J. D. (1984) ^{17}O-water and cyanide ligation by the active site iron of protocatechuate 3,4-dioxygenase. Evidence for displaceable ligands in the native enzyme and in complexes with inhibitors or transition state analogs. *J. Biol. Chem. 259*, 4487−4495.
(79) Burger, R. M., Peisach, J., and Horwitz, S. B. (1981) Activated bleomycin. A transient complex of drug, iron, and oxygen that degrades DNA. *J. Biol. Chem. 256*, 11636−11644.